

## CHAPTER 7

### PYROELECTRIC ENERGY CONVERSION

*Laurent Pilon\** & *Ian M. McKinley*

Mechanical and Aerospace Engineering Department, Henry Samueli School of Engineering and Applied Science, University of California, Los Angeles, CA

\*Address all correspondence to: Laurent Pilon, E-mail: [pilon@seas.ucla.edu](mailto:pilon@seas.ucla.edu)

*This chapter aims to review the fundamental and unique properties of pyroelectric materials and the different strategies using them for direct energy conversion of waste heat into electricity. Pyroelectric energy conversion can be divided into linear and cycle-based methods. Linear pyroelectric energy conversion consists of subjecting a pyroelectric material to periodic heating and cooling in the absence of an electric field bias. It is easy to implement both in terms of hardware and electronics. However, the energy and power densities generated and the associated efficiency are relatively small. Pyroelectric energy conversion cycles consist of performing a closed cycle in the electric displacement  $D$ , electric field  $E$ , temperature  $T$ , and stress  $\sigma$  phase diagram. These cycles typically take advantage of the large change in displacement associated with solid state phase transitions, induced by changes in temperature and/or compressive stress, to achieve large energy and power densities. This chapter presents basic concepts and properties of pyroelectric materials. Then, it thoroughly reviews and critically discusses the practical implementations and performance of linear and cycle-based pyroelectric energy conversion methods proposed to date. Finally, particular attention is paid to experimental demonstrations and performance of the Olsen cycle, also known as the electric Ericsson cycle.*

**KEY WORDS:** *pyroelectric materials, direct energy conversion, waste heat harvesting, ferroelectric materials, Olsen cycle, thermomechanical energy*

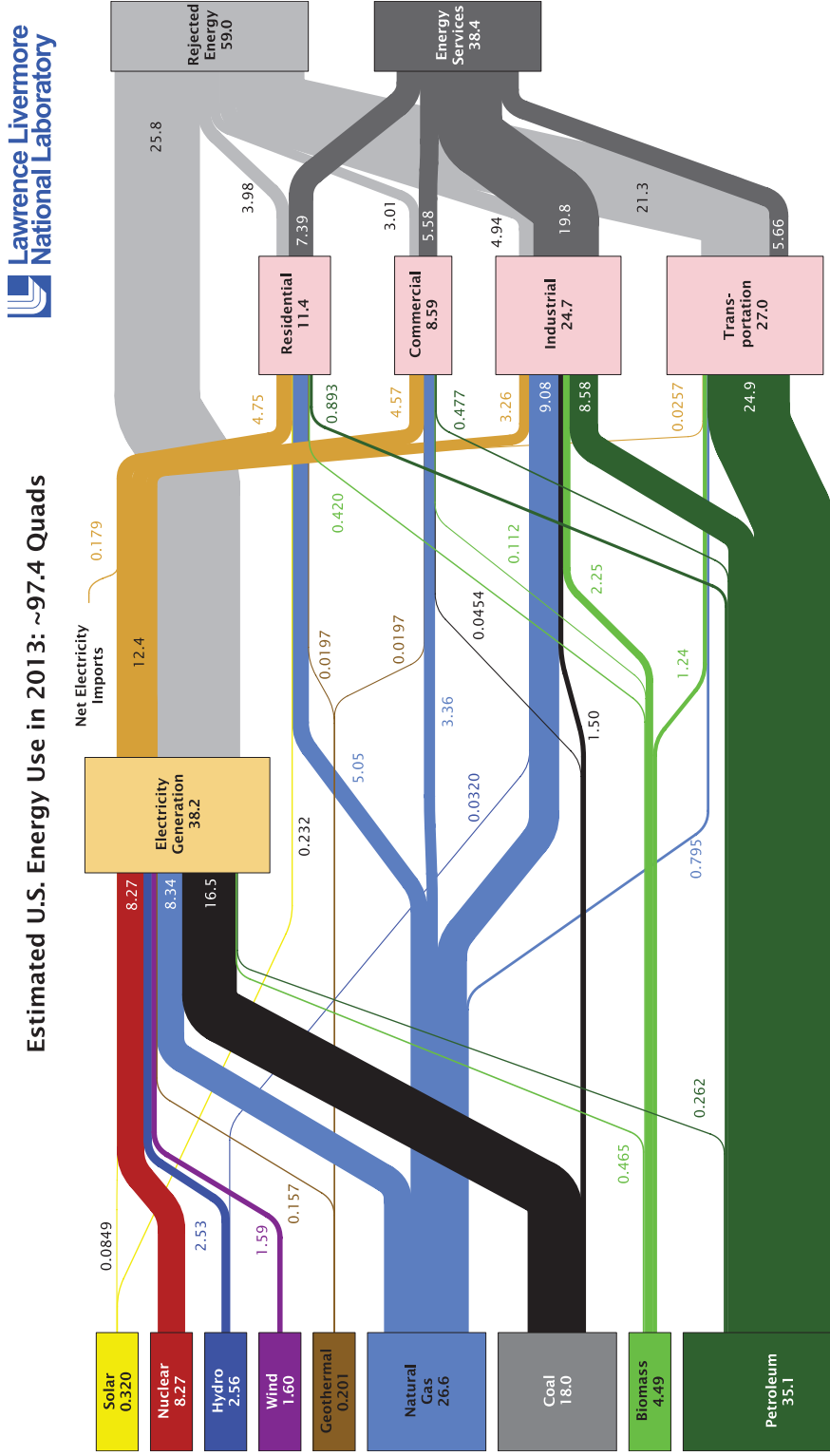
#### 1. INTRODUCTION

Waste heat refers to the thermal energy rejected as a by-product of power, refrigeration, or heat pump cycles as required by the second law of thermodynamics or resulting from irreversible processes (e.g., heat losses, friction). It is often released into the atmosphere, rivers, or oceans in the form of hot exhaust gases or hot water. Figure 1 shows estimates of the energy produced, used, and rejected in the United States in 2013 in quadrillion British thermal units ( $10^{15}$  BTU = 1.05 exajoule).<sup>1</sup> It indicates that only 39% of the energy contained in raw energy sources (e.g., petroleum, natural gas, coal, and nuclear) was useful in residential, commercial, industrial, electricity generation, or transportation applications. The remaining 61% was rejected mainly in the form of waste heat. A wide variety of processes produce large amounts of waste heat. For example, the typical thermal efficiency of an internal combustion engine car is about 30–40%.<sup>2,3</sup> In other words, 60–70% of the energy contained in the fuel is rejected. In fact,  $\sim 35\%$  of the energy in gasoline is lost in

## NOMENCLATURE

$A$	sample surface area, $m^2$	$T_{cold}$	cold temperature reached by the PE, $^{\circ}C$
$b$	sample thickness, m	$T_{Curie}$	Curie temperature, $^{\circ}C$
$c_p$	specific heat, $J/kg \cdot K$	$T_{hot}$	hot temperature reached by the PE, $^{\circ}C$
$C$	capacitance, F	$T_H$	cold source temperature, $^{\circ}C$
$D$	electric displacement, $C/m^2$	$x$	molar fraction
$d_{33}$	piezoelectric coefficient, $C/N$	$x_3$	strain in longitudinal direction, $[= \int_{T_C}^T \alpha(T)] \cdot dT$
$E$	electric field, $V/m$	$V$	voltage, V
$E_b$	electrical breakdown field, $V/m$	$V_1$	voltage across capacitor, V
$E_c$	coercive electric field, $V/m$	$V_2$	voltage across resistor, V
$E_H$	low electric field in Olsen cycle, $V/m$	$\dot{W}_{in}$	mechanical energy input per unit volume, $J/m^3$
$E_L$	high electric field in Olsen cycle, $V/m$	$\dot{W}_e$	electrical power generated by the device, W
$f$	frequency, Hz	$\dot{W}_c$	power consumed for operating the device, W
$I$	electric current, A	$\dot{W}_{net}$	net power from the device ( $\dot{W}_{net} = \dot{W}_e - \dot{W}_c$ ), W
$I_p$	generated electric current, A	<b>Greek Symbols</b>	
$I_L$	leakage current, A	$\alpha$	linear thermal expansion coefficient, $K^{-1}$
$N_D$	energy density, $J/L$	$\epsilon_o$	vacuum permittivity ( $= 8.854 \times 10^{-12} F/m$ )
$p_c$	pyroelectric coefficient, $C/m^2 \cdot K$	$\epsilon_r$	relative permittivity
$P$	polarization density, $C/m^2$	$\epsilon_{r,H}$	relative permittivity at high field
$P_D$	power density, $W/L$	$\eta_d$	device efficiency, %
$P_r$	remanent polarization, $C/m^2$	$\eta_m$	material efficiency, %
$P_s$	spontaneous polarization, $C/m^2$	$\rho$	density, $kg/m^3$
$P_{sat}$	saturation polarization, $C/m^2$	$\sigma$	compressive stress, Pa
$Q$	charge, C	$\sigma_H$	high compressive stress in thermomechanical cycle, Pa
$Q_{in}$	thermal energy input per unit volume, $J/m^3$	$\tau_{ij}$	duration of process $i-j$ , s
$\dot{Q}_{in}$	total heat transfer rate to the device, W		
$R$	resistance, $\Omega$		
$s_{33}$	elastic compliance, $m^2/N$		
$t$	time, s		
$T$	temperature, $^{\circ}C$		
$T_B$	Burns temperature, $^{\circ}C$		
$T_C$	hot source temperature, $^{\circ}C$		

the form of heat to the cooling system and radiator and another 35% through the tailpipe.<sup>3</sup> Similarly, >65% of the energy consumed in the electric generation sector was wasted while this sector contributes the most to raw energy consumption. If the large amount of this ubiquitous waste heat can be efficiently and cost-effectively converted into useful forms of



Source: LLNL 2014. Data is based on DOE/EIA-0035(2014-03), March, 2014. If this information or a reproduction of it is used, credit must be given to the Lawrence Livermore National Laboratory and the Department of Energy, under whose auspices the work was performed. Distributed electricity represents only retail electricity sales and does not include self-generation. EIA reports consumption of renewable resources (i.e., hydro, wind, geothermal and solar) for electricity in BTU-equivalent values by assuming a typical fossil fuel plant "heat rate." The efficiency of electricity production is calculated as the total retail electricity delivered divided by the primary energy input into electricity generation. End use efficiency is estimated as 65% for the residential and commercial sectors, 80% for the industrial sector, and 21% for the transportation sector. Totals may not equal sum of components due to independent rounding. LLNL-MI-410527

**FIG. 1:** Flow chart of the energy produced, used, and rejected in the United States in 2013 (unit in quads, 10<sup>15</sup> Btu) (adapted from the US Department of Energy).<sup>1</sup>

energy, it could contribute to meeting the energy needs of an increasing world population aspiring to higher standards of living. These considerations have brought significant attention to waste heat energy harvesting methods and devices.<sup>4-6</sup>

Waste heat can be divided into three categories: low-, medium-, and high-grade waste heat with temperatures in the range of 25–200, 200–600, and 600–1600°C, respectively.<sup>7</sup> High-grade waste heat can be easily converted efficiently to electricity or hot water for industrial and district heating thanks to cogeneration. By contrast, harvesting medium- and low-grade waste heat is challenging due to the low temperature and the small associated Carnot efficiency. However, technologies exist to convert such waste heat into usable energy, including: (i) Stirling engines,<sup>5</sup> (ii) organic Rankine cycle engines,<sup>4,8</sup> and (iii) thermoelectric generators.<sup>6,9</sup> Organic Rankine cycle and Stirling engines can convert waste heat into mechanical work.<sup>4,5</sup> However, an additional step is required to convert mechanical energy into electricity by means of an electric generator. In addition to the relatively low Carnot efficiency associated with low-grade heat, losses due to friction, heat losses to the surroundings, and gas leakage (in Stirling engine) further reduce their efficiency.<sup>5</sup> Thermoelectric devices utilize the Seebeck effect to directly convert a steady-state temperature difference at the junction of two dissimilar metals or semiconductors into electrical energy.<sup>6</sup> Thermoelectric generators are commercially available but typically have relatively low efficiency and/or are expensive.<sup>6</sup> Alternatively, pyroelectric energy conversion methods use the pyroelectric effect and time-dependent temperature oscillations to create a flow of charge to or from the surface of a pyroelectric material as a result of repeated heating and cooling. Here also, they directly convert low-grade waste heat into electricity.

Pyroelectric materials are dielectric materials with strong temperature-dependent spontaneous polarization, defined as the average electric dipole moment per unit volume in absence of an applied electric field.<sup>10-12</sup> Figure 2 depicts the pyroelectric effect taking place in pyroelectric films.<sup>12</sup> The spontaneous polarization of a bare slab naturally attracts free charges such as electrons and ions to its surface, as shown in Fig. 2(a). Now, let us consider cases when electrodes are attached on both faces of the pyroelectric film and connected to an ammeter. At steady state ( $dT/dt = 0$ ), the spontaneous polarization remains constant and, therefore, no current flows through the ammeter [Fig. 2(b)]. However, as the temperature increases ( $dT/dt > 0$ ), electric dipole moments lose their orientations, leading to a decrease in spontaneous polarization [Fig. 2(c)]. Upon cooling ( $dT/dt < 0$ ), the spontaneous polarization increases and the current reverses sign [Fig. 2(d)]. The electric current  $I_p$  generated by pyroelectric materials during such heating and cooling is given by<sup>13</sup>

$$I_p = Ap_c \frac{dT}{dt} \quad (1)$$

where  $p_c$  is the pyroelectric coefficient. Note that Eq. (1) is not valid for large temperature changes due to nonlinear behavior and potential phase transition(s).<sup>14</sup> The pyroelectric effect has been used for a variety of applications, including motion and fire detection, radiometry, and, infrared imaging.<sup>11,15</sup> Motion and fire detectors use the pyroelectric effect to generate a small current (nA or pA) when an object is at a different temperature than its surrounding. Similarly, pyroelectric materials are used for infrared imaging to differentiate objects by their temperature to within 0.1°C.<sup>11</sup>

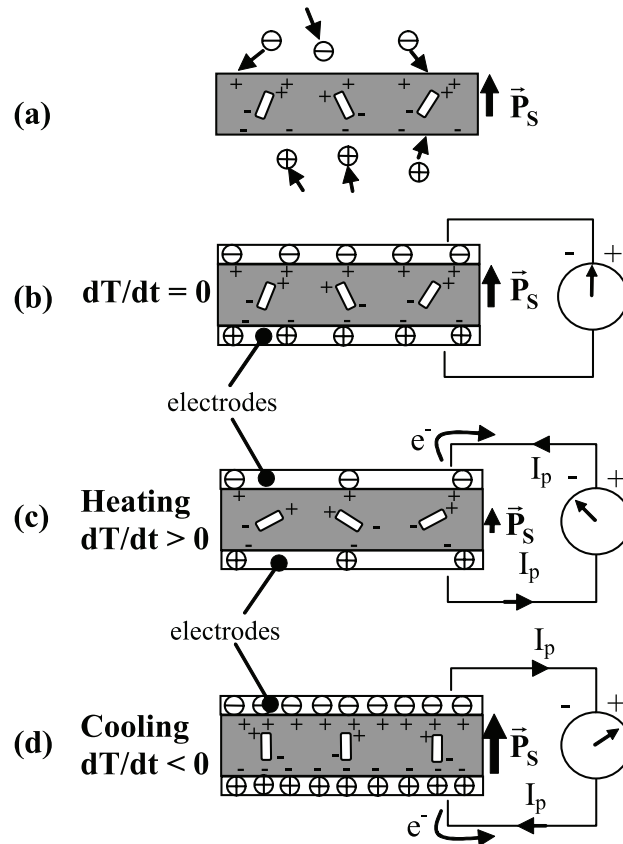


**FIG. 2:** Schematic of a pyroelectric sample (a) by itself and with electrodes and connected to an ammeter (b) at constant temperature, (c) while being heated, and (d) while being cooled (adapted from Lang, 1974).<sup>12</sup>

Pyroelectric energy conversion can be divided into two categories, namely, (i) linear pyroelectric conversion and (ii) solid state thermodynamic cycles. The first category of pyroelectric energy harvesting consists of connecting a pyroelectric material to a resistive electrical load and subjecting it to cyclic temperature fluctuations. In this case, the pyroelectric material typically undergoes temperature fluctuations on the order of 10°C or less. On the other hand, pyroelectric energy conversion cycles consist of subjecting a pyroelectric material to a sequence of thermoelectromechanical processes defining a pyroelectric energy conversion cycles. The latter satisfy the same thermodynamic principles and laws as the traditional thermomechanical cycles used to produce electricity, such as the Rankine cycle.

This chapter aims to review the fundamental properties of selected pyroelectric materials and to discuss different strategies to use their unique properties for direct energy conversion of waste heat into electricity. It also aims to present and critically compare practical implementations and performance of pyroelectric energy conversion methods and devices reported in the literature.

## 2. MATERIALS CONSIDERATIONS

### 2.1 Introduction

Dielectric materials are electrical insulators able to withstand an applied electric field without conducting electricity. They are frequently used in capacitors for electronic circuits. Figure 3 depicts a plane-parallel dielectric film or slab of thickness  $b$  and surface area  $A$  sandwiched between two electrodes subjected to an electric field  $E$  perpendicular to the surface of the slab whose amplitude is given by

$$E = \frac{V}{b} \quad (2)$$

where  $V$  is the applied voltage applied across the slab. The maximum electric field that the material can withstand before becoming conductive is called the electric breakdown field or dielectric strength and denoted by  $E_b$ .<sup>11</sup> The applied electric field causes electric charge to accumulate at the surface of the material. The amount of charge  $Q$  per unit surface area  $A$  is the so-called electric displacement  $D$ . It can be expressed as the sum of (i) the induced polarization due to the displacement of space charges, ions, and electrons in the material caused by the electric field  $E$  and (ii) the polarization due to the spontaneous alignment of dipoles moments according to

$$D = \frac{Q}{A} = \epsilon_0 \epsilon_r E + P \quad (3)$$

where  $\epsilon_r$  is the relative dielectric constant,  $\epsilon_0$  is the vacuum permittivity ( $= 8.854 \times 10^{-12}$  F/m), and  $P$  is the polarization density. In general, the electric displacement  $D$ , electric field  $E$ , and polarization  $P$  are vectors that may not have the same direction. For the sake of simplicity and unless otherwise noted, this chapter considers these different vectors as collinear and normal to the dielectric film's surface.

### 2.2 Crystalline Dielectric Materials

#### 2.2.1 Classification

There are a total of 32 crystal classes of dielectric materials.<sup>11</sup> Twenty of these crystal classes lack a center of symmetry and are called piezoelectrics.<sup>16</sup> Among these 20

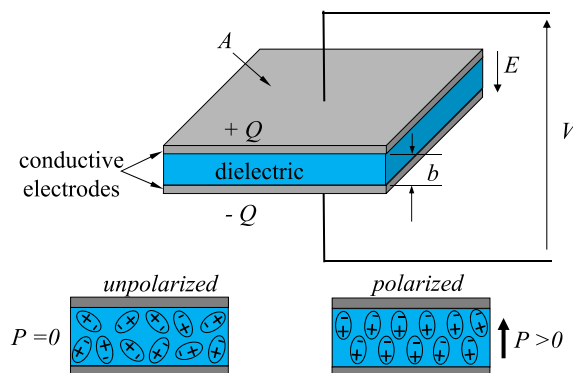


FIG. 3: Schematic of a dielectric material with electrodes subjected to an electric field  $E$ .

piezoelectric crystal classes, ten so-called pyroelectrics demonstrate a unique polar axis and exhibit spontaneous polarization in absence of stress and electric field. A subset of the ten pyroelectric crystal classes, referred to as ferroelectrics, have two or more orientational states that can be switched from one state to another by reversing the electric field.<sup>11</sup> Any two states have identical structure but differ only in their spontaneous polarization. Figure 4 illustrates the relationships between different crystal classes. Note that while all ferroelectrics are pyroelectric and all pyroelectrics are piezoelectric, the converse is not true.

### 2.2.2 Piezoelectrics

A piezoelectric material has the ability to generate an electric potential in response to an applied mechanical stress or vice versa.<sup>16</sup> The application of a mechanical stress or electric field to a piezoelectric material causes a displacement of the centers of mass of positive and negative charges.<sup>17</sup> Because of the absence of a center of symmetry in the structure, the charge displacement is non-symmetrical resulting in an electric dipole moment.<sup>17</sup> If this dipole moment is produced by a mechanical stress, then it will cause a change in charge at the material surface. Conversely, if an external electric field displaces the charges, then the dipole moment produces a mechanical strain causing the material to deform.<sup>17</sup> Small changes in the compressive stress  $\sigma$  applied in the direction parallel to the polarization under constant electric field  $E$  and temperature  $T$  cause linearly proportional changes in the electric displacement  $D$  according to<sup>16,18</sup>

$$dD = d_{33}d\sigma \tag{4}$$

where  $d_{33}$  is the piezoelectric coefficient defined as<sup>16,18</sup>

$$d_{33} = \left( \frac{\partial D}{\partial \sigma} \right)_{E,T} = \epsilon_0 E \left( \frac{\partial \epsilon_r}{\partial \sigma} \right)_{E,T} + \left( \frac{\partial P}{\partial \sigma} \right)_{E,T} \tag{5}$$

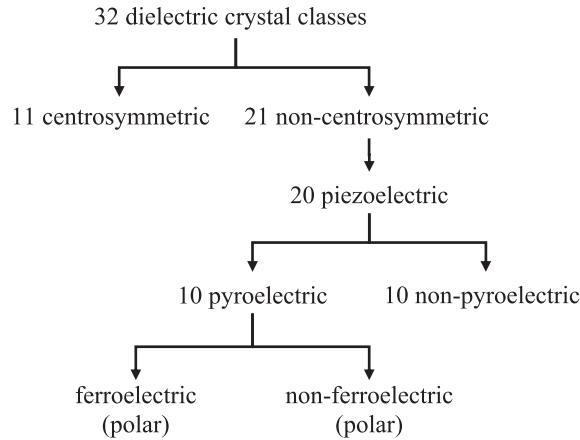


**FIG. 4:** Classification of dielectric crystal symmetry classes depicting the relationship between piezoelectric, pyroelectric, and ferroelectric crystals (adapted from Lang and Das-Gupta, 2001).<sup>11</sup>

Note that, in general, the piezoelectric coefficient is a tensor that can be treated as a scalar corresponding to its element  $d_{33}$  if the electrode surface is normal to the applied stress. Then, the electric current  $I_p$  generated by piezoelectric plane-parallel slab of surface area  $A$  due to changes in compressive stress  $\sigma$  perpendicular to the electrode surface is given by<sup>16,18</sup>

$$I_p = Ad_{33} \frac{d\sigma}{dt}. \quad (6)$$

Note that this linear relationship may not be valid for large changes in compressive stress due to nonlinear behavior in  $d_{33}(\sigma)$ .<sup>19</sup>

### 2.2.3 Pyroelectrics

Pyroelectric materials are characterized by strong temperature-dependent spontaneous polarization due to their particular crystallographic structure.<sup>11,12</sup> Small changes in temperature  $T$  under constant applied normal compressive stress  $\sigma$  and electric field  $E$  cause proportional changes in the electric displacement  $D$  according to<sup>12</sup>

$$dD = p_c dT \quad (7)$$

where  $p_c$  is the pyroelectric coefficient defined as<sup>12</sup>

$$p_c = \left( \frac{\partial D}{\partial T} \right)_{E,\sigma} = \epsilon_0 E \left( \frac{\partial \epsilon_r}{\partial T} \right)_{E,\sigma} + \left( \frac{\partial P}{\partial T} \right)_{E,\sigma} \quad (8)$$

The pyroelectric coefficient  $p_c$  is a vector that can be treated as a scalar if the electrodes are normal to the polarization direction. The electric current  $I_p$  generated during heating or cooling of a pyroelectric plane-parallel slab with electrode surface area  $A$  is given by Eq. (1),<sup>13</sup> which is not valid for large temperature changes due to non-linear behavior.<sup>14</sup> Finally, note that the converse of the pyroelectric effect is the electrocaloric effect. The latter refers to the change in temperature caused by a change in applied electric field under adiabatic conditions.<sup>12</sup>

### 2.2.4 Ferroelectrics and Paraelectrics

Ferroelectric materials have a spontaneous polarization that can be switched between crystallographically defined equilibrium states by reversing the applied electric field  $E$ .<sup>11</sup> Their electric displacement  $D$  features a history-dependent response to variation in external electric field characterized by  $D$  versus  $E$  hysteresis loops. Paraelectric materials are linear dielectric materials that do not have spontaneous polarization (i.e.,  $D = \epsilon_0 \epsilon_r E$ ). However, they can become polarized when subjected to an external electric field.<sup>20</sup> It is apparent in crystal structures where the electric dipole moments are unaligned at zero field but have the potential to align with an external electric field. Compared to ferroelectric materials, paraelectric materials have unordered domains and the internal electric field is weak.<sup>20</sup>

A ferroelectric material may undergo one or more phase transitions between different ferroelectric or paraelectric phases as a result of changing compressive stress  $\sigma$ , temperature

$T$ , and/or electric field  $E$  conditions.<sup>21</sup> The number and nature of such solid state phase transitions are specific to each material and composition. A phase transition of particular interest is the transition between ferroelectric and paraelectric phases. It occurs at the so-called Curie temperature  $T_{Curie}$ . At temperatures below  $T_{Curie}$ , the material is ferroelectric while it is paraelectric above  $T_{Curie}$ . Note that  $T_{Curie}$  depends also on the applied electric field  $E$  and stress  $\sigma$ .

## 2.3 Ferroelectric Hysteresis Loops

### 2.3.1 Definitions

Figure 5 shows typical isothermal bipolar hysteresis curves exhibited by ferroelectric materials in the electric displacement  $D$  versus electric field  $E$  diagram. These so-called D-E loops travel in a counter-clockwise direction and exhibit 180° rotational symmetry about the origin. Starting with an unpolarized material such that  $P_s = 0 \text{ C/m}^2$  at  $E = 0 \text{ V/m}$ , the first increase in electric field poles the material into a ferroelectric material. Indeed, as the electric field increases, ferroelectric domains grow and the material assumes a ferroelectric phase characterized by a spontaneous polarization and D-E hysteresis loops.<sup>22</sup>

For a ferroelectric material at temperature  $T$  under compressive stress  $\sigma$  and large electric field  $E$  applied in the poling direction, Eq. (3) can be written as<sup>11,19</sup>

$$D(E, T, \sigma) = \epsilon_0 \epsilon_{r,H}(T, \sigma)E + P_{sat}(T, \sigma) \tag{9}$$

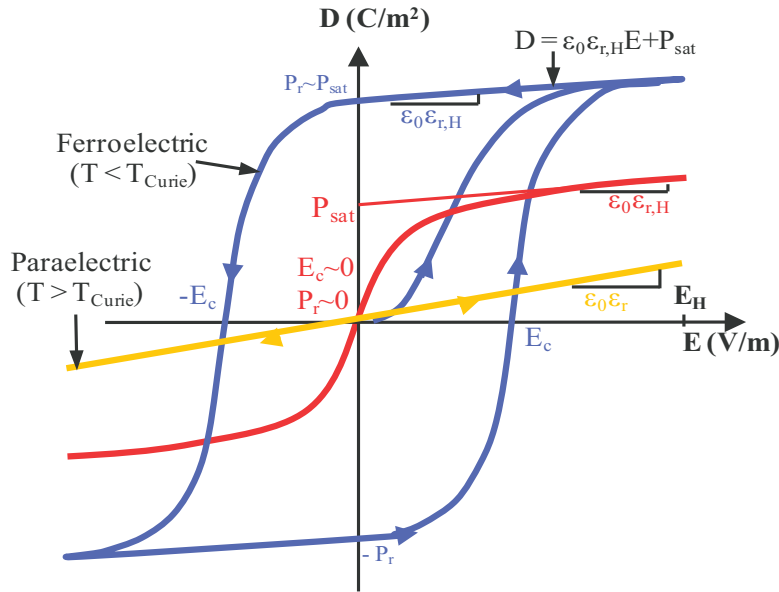


**FIG. 5:** Schematic illustration of electric displacement  $D$  versus electric field  $E$  loops for ferroelectric materials below, around, and well above the Curie temperature  $T_{Curie}$  when they become paraelectric. The D-E loop illustrates the case of electric-field induced phase transition.

were  $\varepsilon_{r,H}(T, \sigma)$  is the high-field relative permittivity of the material at temperature  $T$  and under stress  $\sigma$ . The saturation polarization  $P_{sat}(T, \sigma)$  corresponds to the electric displacement in the linear fit of  $D$  versus  $E$  at large field extrapolated to zero electric field<sup>23</sup> and the slope of this linear fit is the product  $\varepsilon_0 \varepsilon_{r,H}(T, \sigma)$ , as illustrated in Fig. 5. Note that the relative permittivity of a ferroelectric material  $\varepsilon_{r,H}(T, \sigma)$  is assumed to be independent of electric field for large electric fields. This assumption is valid when a single phase is present in a ferroelectric single crystal.<sup>24</sup> Other important features of D-E loops include the remanent polarization  $P_r(T, \sigma)$ , corresponding to the polarization under zero applied electric field, and the coercive field  $E_c(T, \sigma)$ , corresponding to the electric field required to reach zero electric displacement. At temperatures slightly above the Curie temperature  $T_{Curie}(E \simeq 0)$  at low electric field, the material can behave as paraelectric but undergoes electric field-induced phase transition from para-to-ferroelectric and from ferro-to-paraelectric as the electric field is increased or decreased, respectively. Finally, the paraelectric phase prevailing at temperatures above the Curie temperature  $T_{Curie}(E_H)$  at the high electric field  $E_H$  is characterized by zero remanent polarization  $P_r$ , also illustrated in Fig. 5.

### 2.3.2 Effect of Phase Transitions

As a ferroelectric material is heated, the hysteresis curve degenerates into a slimmer D-E loop and the spontaneous polarization  $P_s$  decreases. Beyond the Curie temperature  $T_{Curie}$ , the spontaneous polarization vanishes and the material is paraelectric, as illustrated in Fig. 5.<sup>17,25</sup> The Curie temperature  $T_{Curie}$  can be determined as the temperature at which the dielectric constant  $\varepsilon_r(T, \sigma)$  versus temperature reaches a maximum for a given frequency and applied electric field.<sup>26</sup> It depends on the magnitude, direction, and frequency of the applied electric field  $E$  and on the applied compressive stress  $\sigma$ .<sup>19</sup> It typically increases with increasing electric field  $E$  (Ref. 27) and decreases with increasing compressive stress  $\sigma$  applied in the polarization direction.<sup>28</sup>

### 2.3.3 Leakage Current and Electric Poling

Ideally, the resistance of a pyroelectric material is infinite because it is a dielectric material. In reality, however, the resistance is finite and typically decreases as the applied electric field and/or temperature increase. Leakage current  $I_L$  refers to the phenomenon whereby charges that accumulate at the surface of a dielectric film are transported through its body.<sup>29</sup> In this process, energy is dissipated as Joule heating.<sup>30</sup> Figure 6 represents a pyroelectric element as a simplified equivalent electric circuit consisting of (i) a current generator  $I_p$ , whose direction reverses upon heating and cooling, (ii) a capacitor  $C$ , and (iii) a resistor  $R$  in parallel supporting the leakage current  $I_p$  and decreasing with increasing temperature and electric field. During pyroelectric energy conversion, it is essential to reduce the leakage current to its minimum or else the generated charge cannot be harvested.

Electric poling is a process performed on ferroelectric materials to achieve larger spontaneous polarization and sometimes to induce phase change from paraelectric to ferroelectric. It consists of imposing an electric field to align/order the electric dipole moments of

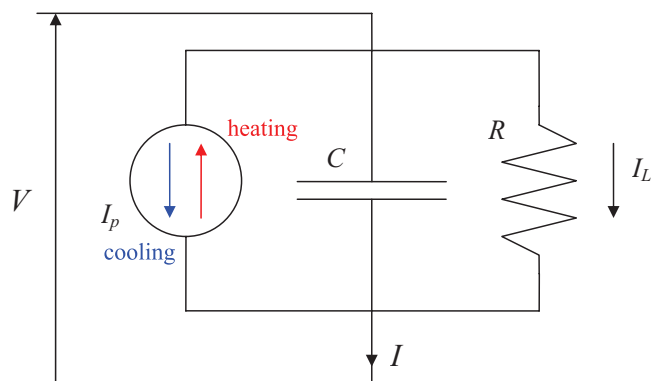


**FIG. 6:** Simplified equivalent circuit of a pyroelectric element during heating and cooling (adapted from Ikura, 2002).<sup>13</sup>

individual crystallite in the direction of the applied electric field.<sup>31</sup> Performing this operation at temperature slightly below the Curie temperature increases the electric dipole mobility and enables one to achieve faster and stronger poling. In turn, the material's electrical resistivity increases and thus the leakage current decreases.<sup>32</sup> Poling has proved particularly important for conditioning ferroelectric polymers, such as P(VDF-TrFE).<sup>29,30,33–35</sup> Note, however, that the polarization of nonferroelectric pyroelectric materials is independent of the electric field.

## 2.4 Selected Pyroelectric Materials

A large number of pyroelectric materials exist, including (i) *minerals* such as tourmaline,<sup>12</sup> (ii) *single crystals* such as lead magnesium niobate-lead titanate (PMN-PT) and lead zirconate niobate-lead titanate (PZN-PT),<sup>36–39</sup> (iii) *ceramics* such as the family of lead zirconium titanate (e.g., PZT and PLZT), barium titanate ( $\text{BaTiO}_3$ ), and lithium titanate ( $\text{LiTiO}_3$ ),<sup>11</sup> (iv) *polymers* such as polyvinylidene fluoride (PVDF) and its co-polymer P(VDF-TrFE), and (v) *biological materials* including bovine phalanx, femur bones, and collagen.<sup>12,40</sup> This section presents the main properties of selected pyroelectric materials that have been used for pyroelectric energy conversion.

### 2.4.1 Lead Zirconate Titanate (PZT) and Relaxor Ferroelectric PLZT Ceramics

Ceramics based on the lead zirconate titanate system  $\text{Pb}[\text{Zr}_x\text{Ti}_{1-x}]\text{O}_3$  (PZT) are the most commonly used ferroelectric materials, because they are mechanically and chemically robust.<sup>12</sup> These materials feature relatively high Curie temperatures between 200 and 500°C, depending on the Zr/Ti ratio or  $x$ . In addition, variation of the Zr/Ti ratio and the addition of possible dopants in PZT may favorably alter its physical properties.<sup>12</sup> Figure 7(a) shows the lattice structure of PZT in cubic (paraelectric) and tetragonal (ferroelectric) phase, and Fig. 7(b) the phase diagram as a function of composition  $x$  and temperature  $T$ .<sup>41</sup> It indicates that PZT has a so-called morphotropic phase boundary (MPB) for  $x$  around 0.4–0.6, referring to the phase transition between rhombohedral and tetragonal phases caused by

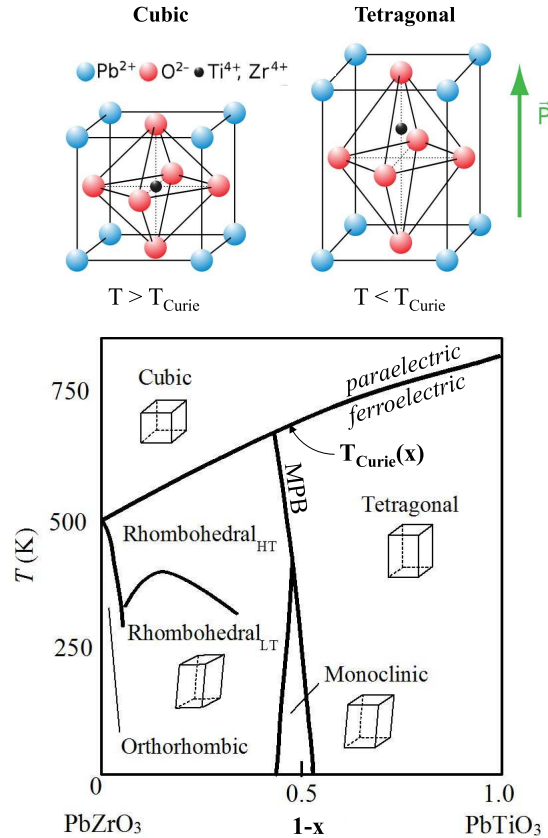


**FIG. 7:** Lattice structure of PZT in cubic and tetragonal phase and phase diagram of PZT illustrating the morphotropic phase boundary (MPB) and the effect of the Zr/Ti ratio  $x$  on the Curie temperature (adapted from Shindo and Narita, 2012).<sup>41</sup>

changes in composition  $x$ .<sup>42</sup> The zero-field Curie temperature of PZT increasing from 225°C (500 K) to ~525°C (800 K) as  $x$  increases from 0 (PbTiO<sub>3</sub>) to 1 (PbZrO<sub>3</sub>).<sup>41</sup>

Relaxor ferroelectrics are different from classical ferroelectric materials in that they exhibit strong frequency dispersion in dielectric permittivity below the temperature corresponding to the maximum permittivity.<sup>43</sup> This dispersion is attributed to the distribution of time constants associated with reorientation of polar nanodomains. The phase transition between ergodic relaxor (nanodomain) and ferroelectric (macrodomain) is field-dependent and occurs at the Curie temperature  $T_{Curie}$ . The material can revert the phase from ferroelectric to ergodic relaxor by heating it above  $T_{Curie}$  and/or by depoling below a critical electric field  $E_{cr}(T)$ . Relaxor ferroelectric materials have been studied extensively due to their (i) exceptional electro-optic properties for optical shutters, (ii) outstanding electrostrictive coefficient for actuators, and (iii) large dielectric constant for capacitors.<sup>43,44</sup>

The  $x/65/35$  PLZT system [Pb<sub>1-x</sub>La<sub>x</sub>(Zr<sub>0.65</sub>Ti<sub>0.35</sub>)<sub>1-x/4</sub>O<sub>3</sub>] is a commonly used relaxor ferroelectric consisting of  $x$  mol.% lanthanum doped into a 65 mol.% lead zirconate PbZrO<sub>3</sub> and 35 mol.% lead titanate PbTiO<sub>3</sub> solid solution. The chemical substitution of

A-site lead  $\text{Pb}^{2+}$  with aliovalent lanthanum  $\text{La}^{3+}$  in PZT introduces dipolar defects that break translational lattice symmetry due to the different sizes and ion valences. It also weakens the coupling between ferroelectric-active oxygen octahedral in the unit cell, thus preventing spontaneous formation of a long-range ordered state.<sup>45</sup> The lanthanum donor dopant contributes to the strong electromechanical coupling and increases structural and compositional disorder responsible for inducing relaxor behavior.<sup>46–48</sup> Furthermore, the lanthanum doping counteracts the p-type electrical conductivity of PZT and increases the electrical resistivity of PLZT materials by at least three orders of magnitude.<sup>49</sup> The phase diagram of  $x/65/35$  PLZT ceramics with  $5 \leq x \leq 9$  mol.% feature rhombohedral crystal symmetry and are near the rhombohedral ferroelectric-mixed ferroelectric/cubic phase boundary.<sup>50,51</sup> The phase transition of the  $x/65/35$  PLZT system depends on the applied electric field, temperature, and frequency.<sup>26,52–54</sup> This ceramic is paraelectric beyond the Burns temperature  $T_B \simeq 350^\circ\text{C}$ , defined as the Curie temperature of the La-free composition.<sup>55</sup> After cooling below  $T_B$ , the material transforms from paraelectric to ergodic relaxor.<sup>43</sup> The Curie temperature  $T_{Curie}$  for the 65/35 Pb/Ti ratio and  $x = 10, 9, 8, 7, 6$ , and 5 mol.% was reported to be  $-25, -10, 65, 150, 240$ , and  $310^\circ\text{C}$ , respectively.<sup>44</sup> An increase in lanthanum dopant concentration hinders the onset of long-range ferroelectric order on cooling.<sup>43</sup> This contributes to Curie temperature reduction from  $310$  to  $-25^\circ\text{C}$  as lanthanum doping level increases from 5 to 10 mol.%.<sup>43</sup> Additionally, the remanent polarization  $P_r$  and dielectric constant  $\epsilon_r$  of rhombohedral ferroelectric  $x/65/35$  PLZT are large compared to other PLZT compositions.<sup>51</sup> Finally, in  $x/65/35$  PLZT, the ferroelectric phase cannot be established spontaneously upon cooling (under zero electric field).<sup>53</sup> However, the ferroelectric phase can be induced and stabilized from the ergodic relaxor phase by applying an external electric field  $E$  greater than  $E_{cr}(T)$ .<sup>56–59</sup>

Figure 8 shows the isothermal bipolar D-E loops of the  $x/65/35$  PLZT system at 0.1 Hz for temperatures between  $-110$  and  $250^\circ\text{C}$ , depending on the composition, and electric field  $E$  ranging from  $-3$  to  $+3$  MV/m, in absence of compressive stress for  $x$  ranging from 5 to 10 mol.%.<sup>60</sup> It illustrates how the material composition can significantly affect the shape of the D-E loops. In particular, increasing  $x$  resulted in a significant decrease in remanent  $P_r$  and saturation  $P_{sat}$  polarization and a decrease in coercive field  $E_c$ , for a given temperature. In addition, for a given composition, the D-E loops overlapped and exhibited square ferroelectric behavior at relatively low temperatures when the remanent polarization was maximum. However, as the temperature increased, the isothermal D-E loops degenerated into narrow and linear loops, particular as ferroelectric to paraelectric phase transition took place.

#### 2.4.2 Single-Crystal PMN- $x$ PT

Single crystals  $\text{PbMg}_{1/3}\text{Nb}_{2/3}\text{O}_3-x\text{PbTiO}_3$  (PMN- $x$ PT) have been widely used in mechanical sensors and actuators and their piezoelectric and dielectric properties have been studied extensively.<sup>21,23,27,28,42,61–69</sup> PMN- $x$ PT possess large piezoelectric constant near the morphotropic phase boundary (MPB).<sup>42</sup> The latter corresponds to  $x$  ranging between 27.5 and 33 mol.%.<sup>62</sup> Compositions near the MPB feature very large piezoelectric and pyroelectric properties interesting for energy conversion.<sup>43</sup> The Curie temperature increases

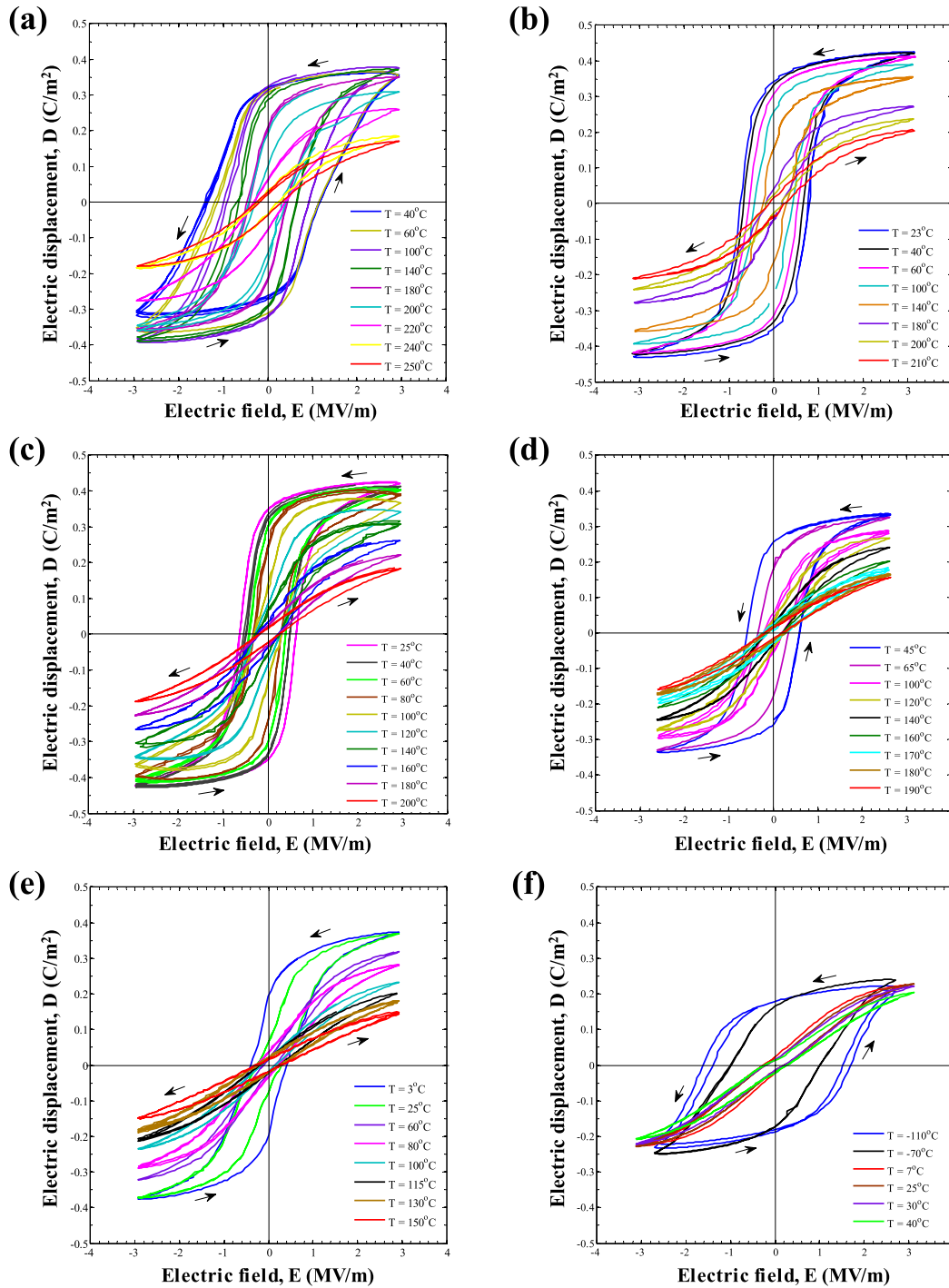


**FIG. 8:** Isothermal bipolar D-E loops of the  $x/65/35$  PLZT system at 0.1 Hz for different temperatures between  $-110$  and  $250^{\circ}\text{C}$  depending on the composition and in absence of compressive stress for  $x$  equal to (a) 5, (b) 6, (c) 7, (d) 8, (e) 9, and (f) 10 mol.%.

with increasing  $\text{PbZrO}_3$  content (i.e.,  $x$ ).<sup>70</sup> For example,  $T_{Curie}$  under zero electric field was reported as 125, 145, and 172°C for PMN-28PT, PMN-32PT, PMN-34PT, respectively.<sup>27,70,71</sup>

Figure 9(a) shows the different phases assumed by [001] PMN-28PT single crystal in the electric field versus temperature (E-T) phase diagram under zero stress.<sup>27</sup> It indicates

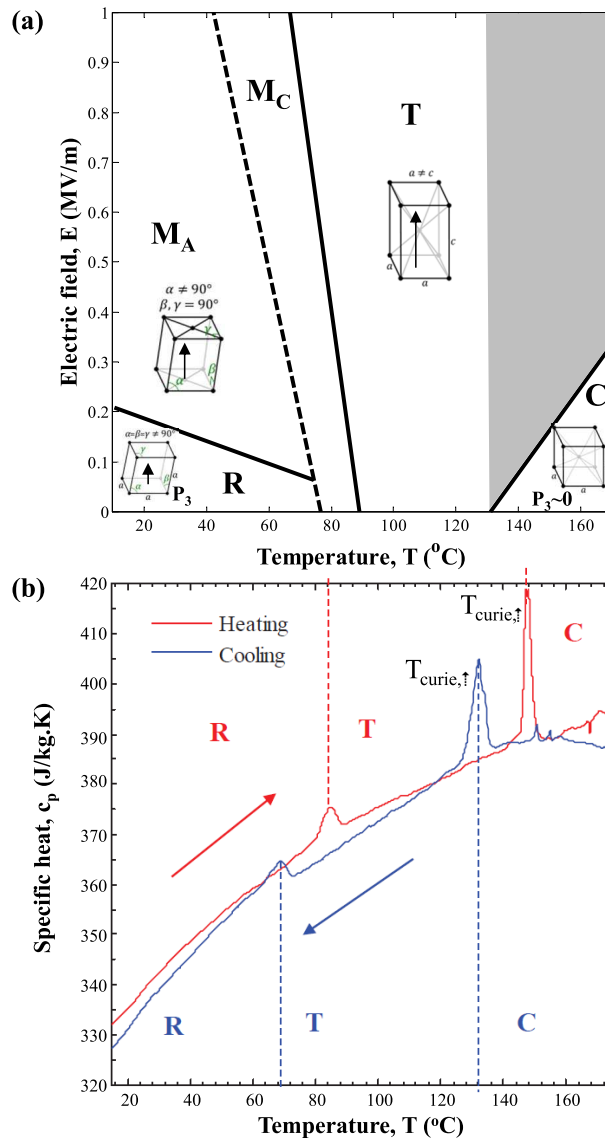


**FIG. 9:** (a) E-T phase diagram of PMN-28PT single crystals under zero stress showing the domains where rhombohedral (R), monoclinic ( $M_A$  and  $M_C$ ), tetragonal (T), and cubic (C) phases prevail. (b) Specific heat  $c_p(T)$  as a function of temperature  $T$  illustrating the different phase transitions of PMN-28PT [(a) adapted from Herklotz et al., 2010 and (b) adapted from McKinley, 2013].<sup>27,74</sup>

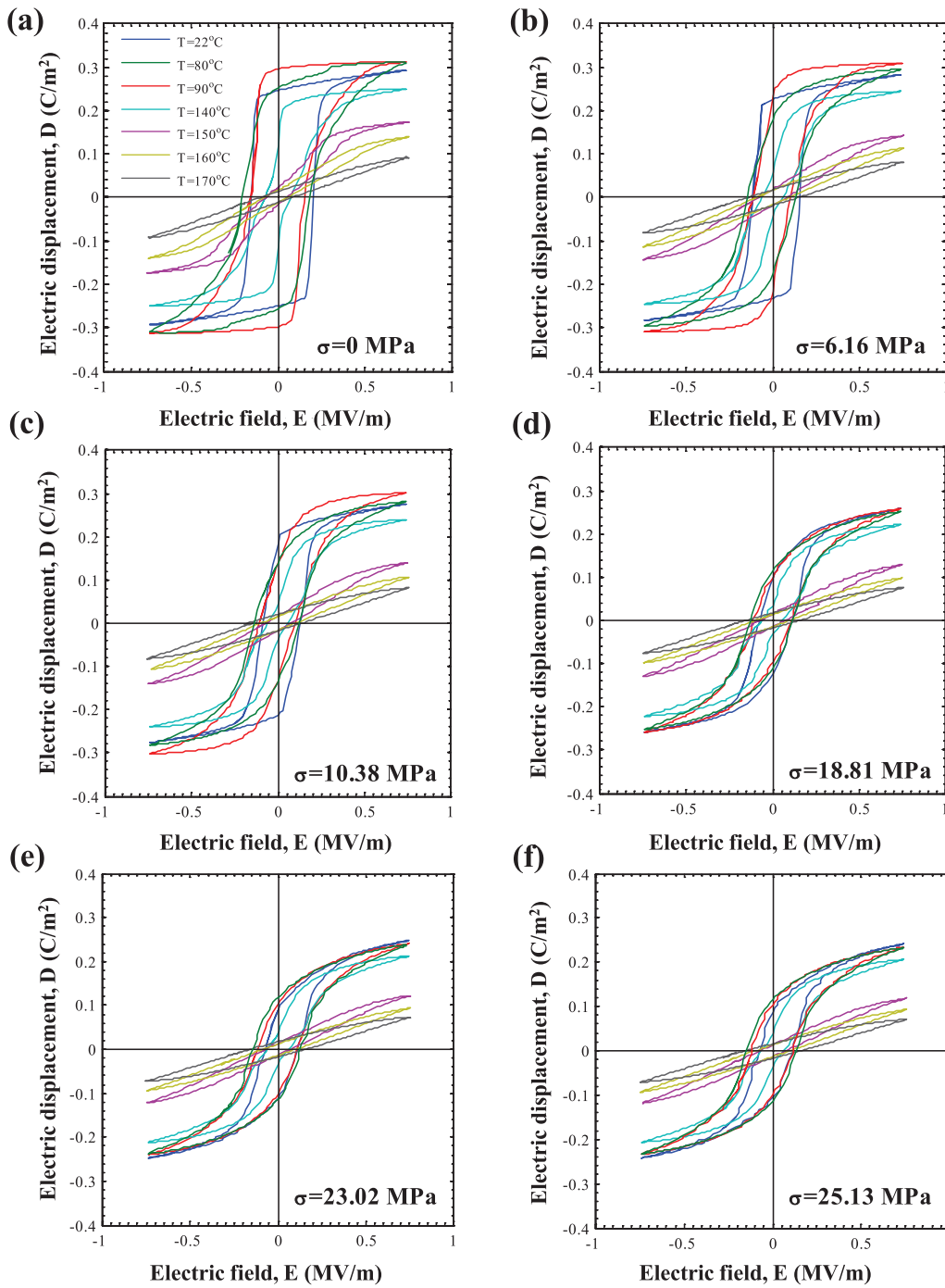
that the material can assume four different crystalline phases in the temperature range from 27 to 177°C and electric field between 0 and 1.5 MV/m.<sup>27</sup> These phases include the rhombohedral (R), monoclinic phases  $M_A$  and  $M_C$ , tetragonal (T), and cubic or pseudocubic phase (C).<sup>27</sup> The associated phase boundaries are both temperature and electric field dependent. At room temperature under zero electric field, the material is in the rhombohedral phase.<sup>72</sup> The Curie temperature at zero field was reported to be  $\sim 125^\circ\text{C}$ ,<sup>27</sup> above which a pseudocubic state existed.<sup>73</sup> Note that the electric breakdown  $E_b$  of PMN- $x$ PT is around 1.0–1.5 MV/m.

Figure 9(b) plots the specific heat  $c_p(T)$  of [001]-poled PMN-28PT as a function of temperature  $T$ .<sup>74</sup> During heating between 15 and 175°C, the PMN-28PT sample exhibited peaks in  $c_p(T)$  at the phase transition temperatures of 85 and 148°C corresponding, respectively, to the rhombohedral to tetragonal and tetragonal to cubic phase transitions.<sup>69</sup> During cooling from 175 to 15°C, the PMN-28PT sample underwent the reverse phase transition sequence with the phase transitions occurring at 132 and 69°C. This illustrates that phase transitions and the Curie temperature depends on whether the sample is heated up or cooled down. In other words, the sharp lines between phases in the phase diagram are used for the sake of clarity but correspond, in reality, to a much more “blurry” phase transition zone.

Figure 10 plots the isothermal bipolar D-E loops for PMN-28PT measured at 0.1 Hz at temperatures between 22 and 170°C, for electric field varying from  $-0.75$  to  $0.75$  MV/m, and under different compressive stress  $\sigma$  between 0 and 25.13 MPa. It illustrates how temperature, electric field, and mechanical loading affect the D-E loops and contribute to polarization switching and phase transitions.<sup>21,28,64,66</sup> In particular, increasing temperature reduced the magnitude of the electric displacement  $D$  to eventually force phase transition to paraelectric phase characterized by small and narrow D-E loops. Similarly, increasing compressive stress reduced the coercive field  $E_c$ , remanent polarization  $P_r$ , and the saturation polarization  $P_{sat}$ .<sup>28,66</sup> In addition, the change in slope observed in the D-E loops as the electric field decreased from 0.75 to 0.0 MV/m, under zero stress, corresponds to electric field-induced phase transitions.<sup>75</sup> According to the E-T phase diagram shown in Fig. 9(a), tetragonal to monoclinic  $M_C$  phase transition occurs at 80°C and 0.4 MV/m. Similarly, the tetragonal to cubic phase transition at temperatures 140, 150, and 160°C occurred at electric fields 0.1, 0.18, and 0.25 MV/m, respectively.<sup>27</sup> At  $T = 170^\circ\text{C}$ , the material remained in the paraelectric pseudocubic phase for all electric fields considered and compressive stress had negligible effect on the D-E loops. Finally, note that the isothermal D-E loops were closed and consecutive D-E loops overlapped for any temperature and compressive stress considered. This indicates that leakage current was negligibly small.

#### 2.4.3 Polymer PVDF and Co-Polymer P(VDF-TrFE)

Polyvinylidene fluoride (PVDF) and its copolymers polyvinylidene fluoride trifluoroethylene [P(VDF-TrFE)] have received significant attention among ferroelectric polymers as they have been used in a wide range of applications.<sup>11,76</sup> The ferroelectric terpolymer P(VDF-TrFE-CFE) has recently generated interest for its narrow hysteresis loops and a faster discharge speed than PVDF and P(VDF-TrFE).<sup>76</sup>



**FIG. 10:** Isothermal bipolar D-E loops of PMN-28PT single crystals at 0.1 Hz for different temperatures between 22 and 170°C under compressive stress  $\sigma$  equal to (a) 0 MPa, (b) 6.16 MPa, (c) 10.3 MPa, (d) 18.81 MPa, (e) 23.02 MPa, and (f) 25.13 MPa (adapted from McKinley, 2013).<sup>74</sup>

First, PVDF has at least four crystal phases, including the  $\alpha$ ,  $\beta$ ,  $\gamma$ , and  $\delta$ -phases whose molecular structures are illustrated in Fig. 11.<sup>77</sup> When cooled from liquid to solid states in the absence of external stresses, PVDF crystallizes into the nonpolar  $\alpha$ -phase. The  $\beta$ ,  $\gamma$ , and  $\delta$ -phases are obtained by simultaneously deforming and poling the polymer.<sup>11,31</sup> Although the  $\alpha$ -phase is paraelectric and more stable, the  $\beta$ -phase exhibits the strongest ferroelectric properties.<sup>31</sup> During the electric poling process, the  $\alpha$ -phase crystals are converted into  $\beta$ -phases by the alignment of dipole moments of individual crystallites in the direction of the applied electric field.<sup>31,78</sup> On the other hand, and unlike PVDF, co-polymer P(VDF-TrFE) spontaneously crystallizes into the ferroelectric  $\beta$ -phase in the absence of external stresses.<sup>79</sup> Repoling P(VDF-TrFE) and P(VDF-TrFE-CFE) occurs spontaneously and requires only cooling below their respective Curie temperature  $T_{Curie}$ . By contrast, repoling PVDF requires mechanical deformation or electric poling yet again. Thus, P(VDF-TrFE) and P(VDF-TrFE-CFE) are preferred for pyroelectric energy conversion subjecting them to numerous heating and cooling cycles.

Co-polymers P(VDF-TrFE) are attractive for their (i) large pyroelectric coefficients, (ii) larger dielectric strength, (iii) low density, (iii) low cost, and (iv) flexibility.<sup>11,80</sup> In addition, P(VDF-TrFE) features a very large electric breakdown field  $E_b$  on the order of 50–100 MV/m (i.e., 50–100 times larger than that of PZT,<sup>81</sup> PLZT, or PMN- $x$ PT, typically around 1–5 MV/m). The Curie temperature of P(VDF-TrFE) is also relatively low compared to that of ceramics PZT and PLZT, making it attractive for low-temperature waste heat harvesting. What's more,  $T_{Curie}$  of P(VDF-TrFE) can be adjusted by varying the VDF/TrFE ratio and the applied electric field. For example,  $T_{Curie}$  increases from 63 to 130°C as the VDF/TrFE ratio increases from 50/50 to 75/25.<sup>82</sup> Note also that the Curie temperature increases with increasing applied electric fields.<sup>79</sup> For example, for 60/40 P(VDF-TrFE)  $T_{Curie}$  increases from  $\sim 70^\circ\text{C}$ , at zero field, to 120°C for a electric field of 52.7 MV/m.<sup>83</sup> However, the maximum electric displacement of P(VDF-TrFE) is around

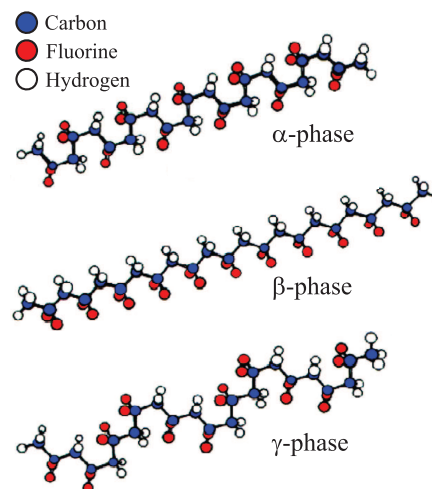


**FIG. 11:** Molecular structure of the three main polymorphic crystalline phases of PVDF namely the  $\alpha$ ,  $\beta$ , and  $\gamma$ -phases (reprinted with permission from Elsevier, Copyright 2010).<sup>77</sup>

0.05–0.1 C/m<sup>2</sup> (Ref. 34) and relatively low compared to that of PLZT and PMN-*x*PT at around 0.3–0.5 C/m<sup>2</sup> (see Figs. 8 and 10).

Moreover, P(VDF-TrFE) co-polymers are prone to leakage current particularly at high electric fields and/or high temperature.<sup>33,34,84–86</sup> Several approaches can be used to reduce leakage current, including (i) purifying pyroelectric materials by eliminating defects in the film,<sup>34,86,87</sup> (ii) baking out or vacuum heating the pyroelectric material before attaching the electrodes in order to evaporate all solvents within the co-polymer as they tend to reduce the polymer resistivity,<sup>33,34</sup> and (iii) poling the pyroelectric element prior to its use to increase its electrical resistance.<sup>30,34,35</sup>

Finally, Table 1 summarizes the advantages and disadvantages of the materials previously discussed for pyroelectric energy conversion. Single crystals and ceramics offer advantages over polymers in that (i) they have large polarization, (ii) they possess significantly lower leakage current thanks to their higher electrical resistivity, and (iii) some of them do not require electrical poling. However, polymer films can sustain significantly larger electric field. Comparing the isothermal D-E loops for PMN-28PT (Fig. 10), *x*/65/35 PLZT (Fig. 8), and P(VDF-TrFE) (Refs. 34 and 86) indicates that although co-polymer P(VDF-TrFE) possess a larger dielectric breakdown than PMN-28PT and PLZT ceramics, the latter feature significantly larger polarization and electric displacement.

### 3. PYROELECTRIC ENERGY CONVERSION

#### 3.1 Linear Pyroelectric Energy Conversion

##### 3.1.1 Principle

A pyroelectric element (PE) consists of a plane-parallel slab or thin film of pyroelectric material with two electrodes deposited on opposite faces used to impose an electric field

**TABLE 1:** Advantages and disadvantages of different pyroelectric materials for pyroelectric energy conversion

Material type	Advantages	Disadvantages
<b>Ceramics</b>	Fast phase transition Chemically stable Adjustable composition High operating temperature	Delicate Susceptible to aging Expensive
<b>Single crystals</b>	Predictable performance Large polarization/displacement Versatile electrode configurations Excellent electromechanical coupling Chemically stable	Small electric breakdown Slow phase transition Expensive Delicate Susceptible to aging
<b>Polymers</b>	Large electric breakdown Inexpensive Operate at low temperatures Large $N_D$ per mass Easy to synthesize	Leakage current Require electric poling Small displacement

and to collect charges (Fig. 3). Linear pyroelectric energy conversion consists of subjecting a pyroelectric element to cyclic temperature fluctuations in the absence of a bias electric field. The PE typically undergoes temperature fluctuations on the order of 10°C or less and behaves in the quasi-linear regime.<sup>35,88–91</sup> In other words, the generated current  $I_p$  is linearly proportional to the time rate of change in temperature  $dT/dt$ , as described by Eq. (1). The PE is connected to a resistive electrical load or to a storage circuit to use or store the electrical energy generated. In order to maximize energy generation, the PE should feature a large pyroelectric coefficient  $p_c$  and large surface area  $A$ .<sup>35</sup> It should also be thermally cycled at high frequency to generate large  $dT/dt$  and as much electrical power as possible. In this case, the pyroelectric element should also have small thermal inertia. This can be achieved by considering materials with low heat capacity, defined as the product of specific heat  $c_p$ , density  $\rho$ , and volume of the PE. Conditions for large surface area and small volume suggest the use of thin films, as illustrated by Hsiao and Jhang<sup>90</sup> with PZT.

### 3.1.2 Performance

Two figures of merit (FOM) have been proposed to quantify the performance of pyroelectric materials for linear pyroelectric energy conversion, namely  $F_E$  (Ref. 92) and  $k^2$  (Ref. 93) defined as

$$F_E = \frac{p_c^2}{\varepsilon_0 \varepsilon_r} \quad \text{and} \quad k^2 = \frac{p_c^2 T_H}{\rho c_p \varepsilon_0 \varepsilon_r} \quad (10)$$

where  $p_c$  is the pyroelectric coefficient,  $\varepsilon_0 \varepsilon_r$  is the permittivity,  $\rho$  is the density,  $c_p$  is the specific heat of the pyroelectric material, and  $T_H$  is the temperature of the hot source. The FOM  $F_E$  represents how much electrical power a pyroelectric material can harvest from the hot source while  $k^2$  is a dimensionless electrothermal coupling factor representing how effectively a pyroelectric material converts thermal energy into electrical energy. An alternative FOM has been recently proposed as<sup>94</sup>

$$F'_E = \frac{p_c^2}{(\rho c_p)^2 \varepsilon_0 \varepsilon_r}. \quad (11)$$

Note that these FOM are independent of frequency and film thickness. However, these parameters are known to affect the power generated.<sup>35,90,95,96</sup>

### 3.1.3 Demonstration

Table 2 summarizes the various experimental demonstrations of linear pyroelectric energy conversion reported in the literature, in chronological order.<sup>35,91,95,97–102</sup> It includes the PE material and dimensions, the hot and cold sources, the minimum and maximum temperatures reached by the PE, the maximum heating/cooling rates  $dT/dt$ , and the peak areal ( $\mu\text{W}/\text{cm}^2$ ) and volumetric (W/L) power densities as well as the energy density (J/L/cycle) whenever available or applicable. Most studies used commercial PZT,<sup>35,95,97–100</sup> while a few investigated PMN-PT (Refs. 95 and 97) and PVDF (Refs. 35, 97, and 101).

**TABLE 2:** Comparison of peak power and energy densities achieved by linear pyroelectric energy conversion with different materials, heating and cooling methods, temperature ranges, and heating/cooling rates. Here, no bias electric field was applied to the PE

Material	Thickness ( $\mu\text{m}$ )	Surface area ( $\text{cm}^2$ )	Hot/cold sources	$T_{\text{cold}}$ ( $^{\circ}\text{C}$ )	$T_{\text{hot}}$ ( $^{\circ}\text{C}$ )	$(dT/dt)_{\text{max}}$ ( $^{\circ}\text{C/s}$ )	Peak areal			Energy density ( $\text{J/L/cycle}$ )	Ref.
							power ( $\mu\text{W/cm}^2$ )	power ( $\text{W/L}$ )	power ( $\text{W/L}$ )		
PZT and PVDF	100	16	hair blower	27	67	N/A	0.013	$1.25 \times 10^{-3}$	0.1	35	
PZT-5A	150	1.44	resistance heater	30	103	15.6	0.20	0.013	N/A	97	
PMN-30PT	273	0.98	resistance heater	22	104	14	0.33	0.012	N/A	97	
PVDF	110	1.96	resistance heater	30	141	20	0.12	0.011	N/A	97	
PZT	250	1.59	heat lamp/air	32	40	8.5	0.11	$4.48 \times 10^{-3}$	0.0011	95	
pre-stressed PZT	200	1.44	heat lamp/air	32	40	8.5	0.13	$6.31 \times 10^{-3}$	0.0016	95	
PMN-30PT	270	0.98	heat lamp/air	32	40	8.5	0.23	$8.64 \times 10^{-3}$	0.0021	95	
PZT	250	1	hot and cold plates	25	121	N/A	4.40	$1.76 \times 10^{-2}$	0.0926	98	
PVDF	110	9	hot and cold water	0	80	N/A	14.00	1.080	N/A	101	
PZT-5H	500	4	sun/Al heat sink	50	110	40	21.05	0.421	6.927	100	
PZT	200	0.81	heat lamp/air	65	75	0.007	2.47	0.123	N/A	90	
PZT-5A	200	0.34	heat lamp/air	38	46	4	8.30	0.415	8.30	102	
PZT	140	4.52	heat lamp/air	27	43	0.53	4.20	0.3	30.00	99	

Different circuits exist to harvest the energy generated by linear pyroelectric converters.<sup>35,89</sup> The most commonly used electric circuit, to measure and/or to collect the electrical energy generated, consisted of a full-wave rectifier bridge circuit connected to a capacitor for storage.<sup>90,96,99,101–103</sup> This circuit converts the AC current generated by the pyroelectric element into a DC voltage conditions for storage. In addition, the so-called synchronized switch harvesting on inductor (SSHI) circuit has been demonstrated experimentally to increase the energy harvested by a factor of 2.5 compared to the full-wave rectifier circuit.<sup>89</sup> It consists of an inductor in series with an electronic switch that is always open except in the vicinity of temperature extremes.<sup>89</sup> Finally, less frequently, an operational amplifier connected in parallel to the PE and a load resistor have been used. Here, the resistance can be varied for impedance matching.<sup>95,100</sup>

The maximum power generated per unit surface area of pyroelectric material was reported as  $21 \mu\text{W}/\text{cm}^2$  using  $500 \mu\text{m}$  thick PZT-5H films exposed to solar radiation concentrated with a Fresnel lens as the heat source.<sup>100</sup> A wind turbine actuated a gear box system to periodically obstruct the incident solar radiation and create periodic temperature oscillations in the PE. Leng et al.<sup>101</sup> used also the linear pyroelectric effect to produce electrical power from hot water, at up to  $80^\circ\text{C}$ , and cold water, around  $0^\circ\text{C}$ , alternatively flown over a  $110 \mu\text{m}$  thick PVDF film with surface area of  $3 \times 3 \text{ cm}^2$  with  $10 \mu\text{m}$  Cu electrodes at a frequency of up to  $5\text{--}10 \text{ Hz}$ . The maximum areal and volumetric ( $\mu\text{W}/\text{cm}^3$  or  $\text{W}/\text{L}$ ) power densities generated by their system were respectively  $14 \mu\text{W}/\text{cm}^2$  or  $1.08 \text{ W}/\text{L}$  [erroneously reported as  $1.08 \text{ W}/\text{cm}^3$  (Ref. 104)]. This was the largest power density reported to date for linear pyroelectric energy conversion. Note that, in all cases, the maximum temperature was maintained below the Curie temperature presumably to avoid depoling of the pyroelectric film. In addition, most studies did not report the efficiency of the overall system except for Zhang et al.,<sup>99</sup> who reported an efficiency of  $6 \times 10^{-5}\%$ .

Finally, simple thermal and electric circuit models have been developed to predict the temporal evolutions of voltage across the storage capacitor.<sup>99</sup> and temperature oscillations in the PE.<sup>96,98,105–107</sup> They have shown very good agreement with experimental measurements.<sup>98,99,106</sup>

### 3.1.4 Challenges and Improvements

Overall, linear pyroelectric power generation can be used with any pyroelectric material. It is relatively easy to implement experimentally in terms of device design, assembly, and electric circuit. However, it typically does not take advantage of the large change in polarization experienced by ferroelectric materials as a result of phase transition to paraelectric. This is due to the fact that the pyroelectric materials considered (e.g., PZT, PVDF) lose their spontaneous polarization when heated above their Curie temperature and do not recover it during subsequent cooling below the Curie temperature without a bias electric field. As a consequence, linear pyroelectric energy generation suffers from low energy and power densities, and low efficiency.

Improvements have also been sought in the geometry of pyroelectric elements and of their electrodes. For example, Hsiao et al.<sup>105</sup> isotropically etched quasi-spherical cavities with a square footprint on one face of a  $200 \mu\text{m}$  PZT film with meshed electrodes.

Similarly, Hsiao et al.<sup>96</sup> cut 200  $\mu\text{m}$  wide and 50–150  $\mu\text{m}$  deep rectangular trenches using a precision dicing saw on one face of a 200  $\mu\text{m}$  PZT film. Here, Au electrodes were deposited by e-beam evaporation on the top surface of the film and trenches electrically connected to one another with silver paste. Their results suggest that the presence of trenches enhances the heating and cooling rates of the PE by acting as parallel-plate fins. However, it remains unclear whether the energy and/or power generated improved as some active material was removed. Further exploring the structure of the PE surface, Hsiao and Siao<sup>103</sup> demonstrated that replacing planar conformal electrodes on a plane-parallel film with three-dimensionally structured electrodes could increase the energy and power densities of linear pyroelectric energy conversion. The increase in energy generation was attributed to the enhanced heat transfer induced by the electrodes' patterned surfaces.

## 3.2 Pyroelectric Energy Conversion Cycles

### 3.2.1 Introduction

As previously discussed, pyroelectric energy conversion cycles consist of subjecting a pyroelectric element to a sequence of thermoelectromechanical processes describing a closed path in the three-dimensional D-E-T or in the four-dimensional D-E-T- $\sigma$  phase diagram. Pyroelectric energy conversion cycles may also take advantage of solid state phase transition(s) induced by changes in temperature, electric field, and/or compressive stress, including the ferroelectric-to-paraelectric phase transition, previously discussed. This section introduces the principles of several pyroelectric energy conversion cycles reported in the literature.

### 3.2.2 Clingman Cycle

Pyroelectric energy conversion was explored using the Clingman cycle in the 1960s.<sup>108–110</sup> Figure 12 illustrates the Clingman cycle in a D-E diagram. This cycle is implemented as follows:

1. Initially, the PE is at  $T_{cold}$  slightly below  $T_{Curie}$  with both zero applied electric field  $E$  and electric displacement  $D$ .
2. Then, the electric field is isothermally increased from zero to  $E_2$  corresponding to  $D$  increasing from zero to  $D_2$ .
3. The PE is heated from  $T_{cold} \sim T_{Curie}$  to  $T_{hot} > T_{Curie}$  at constant electric displacement  $D_2$  (open circuit). As a result, the electric field increases from  $E_2$  to  $E_3$ .
4. Afterward, the PE is isothermally discharged at temperature  $T_{hot}$  until both  $D$  and  $E$  equal zero.
5. Finally, the PE is cooled to its original temperature  $T_{cold} \sim T_{Curie}$  to close the cycle. This provides a clockwise cycle in the D-E diagram corresponding to positive electric work performed by the PE.

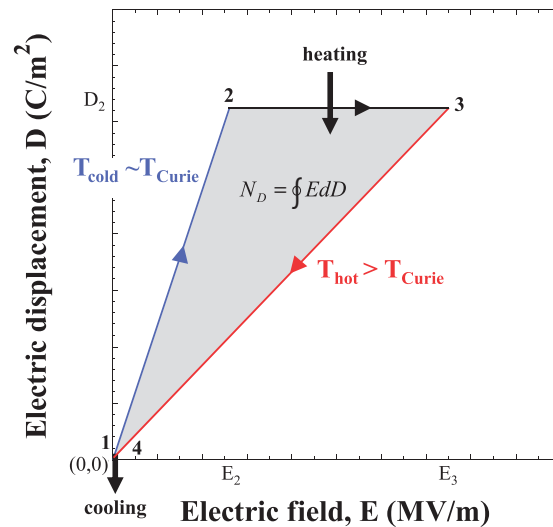


**FIG. 12:** Pyroelectric energy conversion cycle used by Clingman and Moore<sup>108</sup> in the D-E diagram around the Curie temperature.

Theoretical predictions of the efficiency of the Clingman cycle fell below 1%,<sup>108–110</sup> mainly due to the fact that “the energy required to increase the temperature of the lattice is nearly always much larger” than the energy required to release electric charges.<sup>109</sup> The very low theoretical efficiencies discouraged further research on energy harvesting with pyroelectric materials until the late 1970s. However, Van der Ziel<sup>110</sup> made use of Eq. (1) to calculate the pyroelectric current, which is only valid for linear behavior and relatively small changes in temperature.<sup>14</sup> In fact, it has been shown that when the temperature varies by more than several mK, the relationship between current and temperature is no longer linear.<sup>14</sup> Moreover, Hoh<sup>111</sup> suggested that the previous theoretical calculations “suffer from unfortunate choices of material parameters” and that an efficiency of 5.6% can be achieved using lead titanate  $\text{PbTiO}_3$  with a temperature span of  $\Delta T = 30^\circ\text{C}$  and an electric field change of  $\Delta E = E_3 - E_2 = 10^7 \text{ V/m}$ .

Finally, Childress<sup>112</sup> theoretically considered a pyroelectric cycle based on Clingman cycle but such that (i) a voltage was applied during process 3–4, preventing the electric field from reaching zero so as to avoid depoling, and (ii) the PE was open circuited during the cooling process 4–1 so that  $E$  decreased while maintaining a constant  $D$  during this process. Here also, the author considered a thermodynamic efficiency of 0.5% for  $\text{BaTiO}_3$  between 120 and  $150^\circ\text{C}$ , to be too low to have any further interest. In fact, to the best of our knowledge, the Clingman and Childress cycles have never been demonstrated experimentally.

### 3.2.3 Olsen Cycle

The Olsen cycle was developed between 1978 and 1985 by Olsen and Bruno,<sup>83</sup> Olsen and Brown,<sup>115</sup> Olsen and Evans,<sup>116</sup> and Olsen et al.<sup>81,113,114,117</sup> It consists of two isothermal and two isoelectric processes performed on a pyroelectric element.<sup>113</sup> It is analogous to the

Ericsson cycle defined in the pressure versus specific volume phase diagram of a working fluid.<sup>113</sup> Note that it has also been termed as the electric Ericsson cycle<sup>81</sup> or the Ericsson cycle.<sup>118–120</sup> However, we find this terminology confusing and prefer to call the cycle by its inventor's name,<sup>121–123</sup> as also adopted by other groups.<sup>79,100,124</sup>

Figure 13 shows typical isothermal bipolar hysteresis curves plotting electric displacement  $D$  versus electric field  $E$  exhibited by ferroelectric materials at two different temperatures  $T_{cold}$  and  $T_{hot} > T_{Curie}$ . It also illustrates the four processes constituting the Olsen cycle. Process 1–2 consists of charging the pyroelectric element at  $T_{cold}$  by increasing the applied electric field from  $E_L$  to  $E_H$ . Process 2–3 discharges the PE by heating it from  $T_{cold}$  to  $T_{hot}$  under constant electric field  $E_H$ . Process 3–4 reduces the electric field from  $E_H$  to  $E_L$  under isothermal conditions at  $T_{hot}$ . Finally, process 4–1 closes the cycle by cooling the PE from  $T_{hot}$  to  $T_{cold}$  under constant electric field  $E_L$ . In other words, the principle of the Olsen cycle is to charge a capacitor via cooling at small electric field and to discharge it under heating at large electric field. Note that the pyroelectric element is subjected to temperature fluctuations on the order of 50–100°C, resulting in nonlinear behavior. In addition, these processes are performed under zero mechanical stress.

Here also, the area enclosed by the four processes of the Olsen cycle in the D-E diagram depicted in Fig. 13 corresponds to the material energy density  $N_D$ . This indicates that  $N_D$  can be maximized by (i) increasing the change in electric displacement  $D$  as the material temperature varies between  $T_{hot}$  and  $T_{cold}$  and/or by (ii) increasing the electric field span ( $E_H - E_L$ ). First, in order to maximize the change in  $D$ ,  $T_{hot}$  should be higher than the Curie temperature  $T_{Curie}$  at  $E_H$ . In addition,  $T_{cold}$  should be chosen so that the material exhibits the largest electric displacement in the range  $E_L$  to  $E_H$ . Second, to maximize the

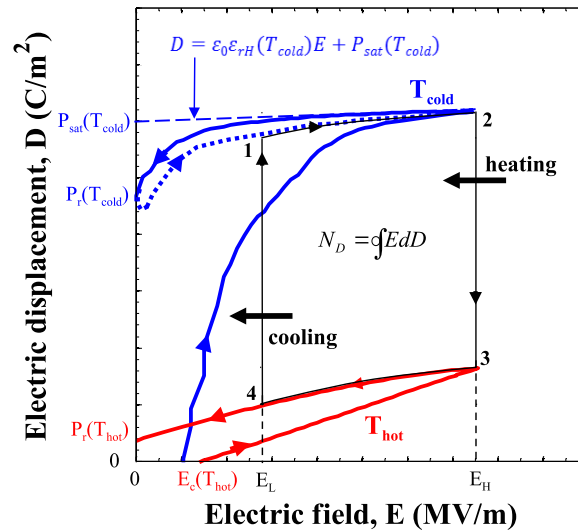


**FIG. 13:** Isothermal bipolar D-E loops for a typical pyroelectric material at temperatures  $T_{hot}$  and  $T_{cold}$  under zero stress  $\sigma = 0$  Pa, along with the Olsen cycle. The electrical energy density  $N_D$  generated per unit volume of material per cycle is represented by the area enclosed between 1-2-3-4.

electric field span ( $E_H - E_L$ ), the pyroelectric material should possess a large electric breakdown field  $E_b$ , whereas  $E_L$  should be as low as possible yet above the electric field required for poling at  $T_{cold}$ . The electric field required for poling is typically slightly larger than the coercive electric field  $E_c$ .<sup>27</sup> Note, however, that these options are limited by the number of thermal cycles and by the electric field that the material can sustain. Excessive and/or repeated temperature swings or temperature gradient and large electric field can lead to premature cracking and failure of the pyroelectric material and/or its electrodes.<sup>125</sup>

Finally, the Olsen cycle has been investigated extensively and demonstrated on PZT,<sup>113–115</sup> P(VDF-TrFE) with different VDF/TrFE ratios,<sup>29,33,126</sup> PMN-PT,<sup>127,128</sup> PZN-PT,<sup>129</sup> various composition of PLZT,<sup>60,125</sup> and BaTiO<sub>3</sub>.<sup>120</sup> This cycle will be discussed in more details in Section 4.

### 3.2.4 Thermomechanical Cycle

#### 3.2.4.1 Principle

The Olsen cycle takes advantage of the large changes in polarization caused by ferroelectric to paraelectric phase transition. However, it relies on heat transfer to drive this phase transition. Unfortunately, heating and cooling are inherently slow processes. To address this limitation, McKinley et al.<sup>130</sup> developed a pyroelectric energy conversion cycle working in the four-dimensional D-E-T- $\sigma$  phase diagram. It uses uniaxial compressive stress in addition to thermal and electric field cycling to rapidly force the pyroelectric material into a specific phase. In other words, they combined piezoelectric and pyroelectric energy conversions and were able to increase the cycle frequency by several orders of magnitude.

Figure 14 shows this thermomechanical power cycle projected onto the D-E plane overlaid with the corresponding bipolar D-E loops at cold temperature  $T_{cold}$  under zero

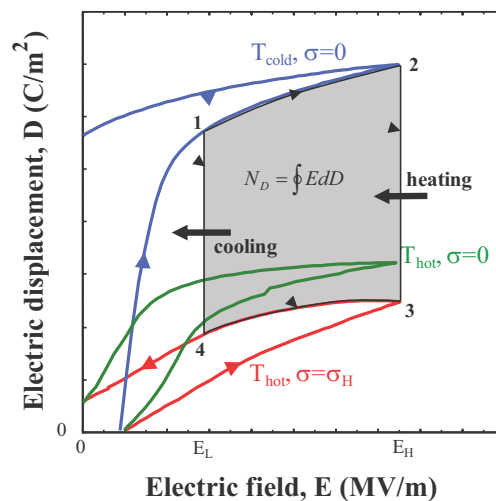


**FIG. 14:** Two-dimensional projections of the thermomechanical pyroelectric energy conversion cycle in the D-E plane and electric displacement versus electric field loops at  $T_{cold}$  for uniaxial stress  $\sigma = 0$  and at  $T_{hot}$  for  $\sigma = 0$  and  $\sigma_H$  (adapted from McKinley, 2014).<sup>130</sup>

stress and at hot temperature  $T_{hot}$  under compressive stress  $\sigma_H$ . Process 1–2 consists of an isothermal increase in electric field from  $E_L$  to  $E_H$  at  $T_{cold}$  in the absence of compressive stress. Process 2–3 simultaneously compresses and heats up the pyroelectric element at  $\sigma_H$  and up to  $T_{hot}$ . Process 3–4 corresponds to an isothermal decrease in electric field from  $E_H$  to  $E_L$  at  $T_{hot}$  under compressive bias stress  $\sigma_H$ . Finally, process 4–1 closes the cycle by simultaneously cooling the pyroelectric element to  $T_{cold}$  and removing the mechanical loading under constant electric field  $E_L$ . Figure 14 also suggests that the thermomechanical cycle extends beyond the bounds of the Olsen cycle confined to the area between the isothermal D-E loops at  $T_{cold}$  and  $T_{hot}$  both under no stress (i.e.,  $\sigma = 0$  Pa). Finally, this cycle has been demonstrated experimentally using single crystal PMN-28PT.<sup>130</sup>

### 3.2.4.2 Implementation

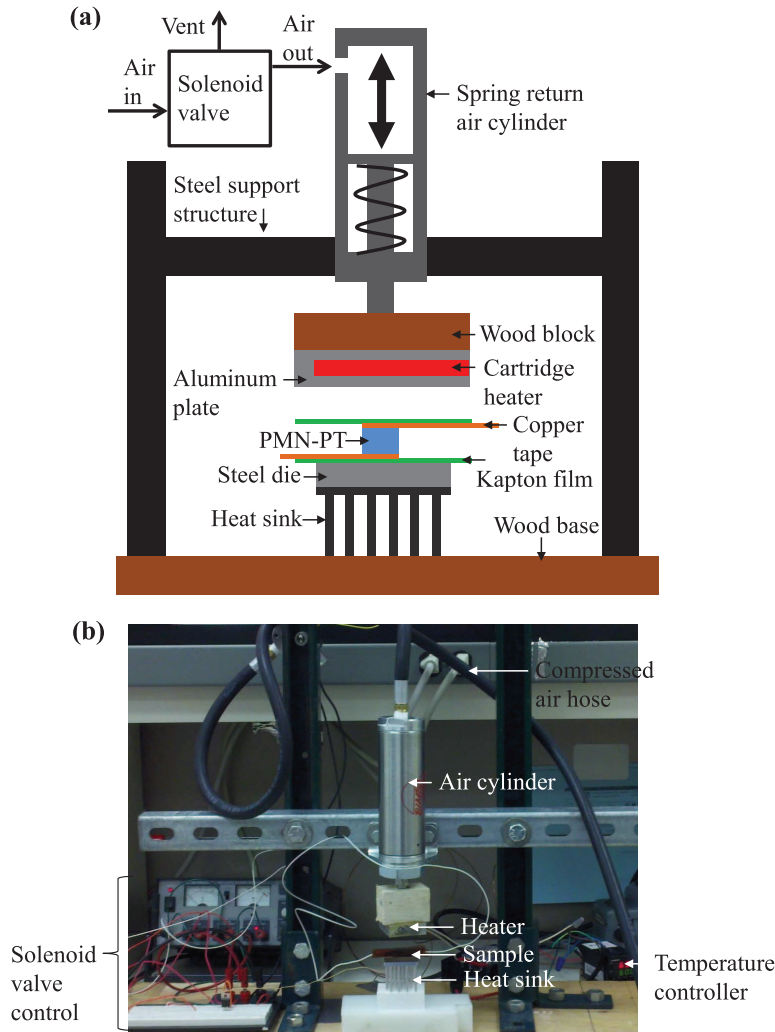
Figure 15(a) is a schematic and Fig. 15(b) is a photograph of the thermomechanical system implementing the above thermomechanical power cycle.<sup>130</sup> It consisted of a spring return air cylinder vertically actuated using compressed air controlled by a solenoid valve to apply the compressive stress  $\sigma_H$ . The heat source consisted of a thick aluminum plate maintained at constant temperature  $T_H$ . The cold source was an aluminum heat sink passively maintained near room temperature  $T_C$ . Note that the cold and hot temperatures reached by the PE differed from  $T_C$  and  $T_H$ . They also depended strongly on the operating frequency.<sup>130</sup> The PE was electrically insulated from the metallic heat source and sink by a thin Kapton film.

Figure 16 depicts, in the D-E diagram, the actual thermomechanical power cycle performed at 0.025 Hz between cold and hot source temperatures  $T_C = 22^\circ\text{C}$  and  $T_H = 187^\circ\text{C}$  corresponding to sample temperatures  $T_{cold} = 59^\circ\text{C}$  and  $T_{hot} = 129^\circ\text{C}$ . The electric field was cycled between  $E_L = 0.2$  MV/m and  $E_H = 0.75$  MV/m. A compressive stress of  $\sigma_H = 18.81$  MPa was applied during processes 2–3 and 3–4. Figure 16 also shows the isothermal bipolar D-E loops collected independently at temperatures near these values of  $T_{hot}$  and  $T_{cold}$  and under compressive stress 0 and  $\sigma_H$ . The power cycle shown in Fig. 16 was vertically translated to match the electric displacement of the D-E loop for  $T_{hot}$  and  $\sigma_H$  at  $E_H$  (state 3), as performed by Olsen and Evans.<sup>116</sup> Figure 16 also suggests that the Olsen cycle performed under similar operating temperatures and electric fields would yield much smaller energy densities considering the area bounded by the D-E loops at temperatures  $T_{cold}$  and  $T_{hot}$ .<sup>128</sup>

### 3.2.5 Performance Metrics

The energy density  $N_D$  generated during the above pyroelectric energy conversion cycles is defined as the electrical energy produced per unit volume of the material per cycle. It is represented by the area enclosed by the clockwise cycle in the D-E diagram (i.e.,  $N_D$  is positive). It is expressed in J/L/cycle (1 J/L/cycle = 1 mJ/cm<sup>3</sup>/cycle) and defined as follows:<sup>113</sup>

$$N_D = \oint E dD \quad (12)$$



**FIG. 15:** (a) Schematic and (b) photograph of the thermomechanical subsystem used to create the periodic temperature oscillations and to apply compressive stress during the thermoelectromechanical power cycle depicted in Fig. 14 (adapted from McKinley, 2014).<sup>130</sup>

The corresponding power density  $P_D$  is the amount of energy generated by the pyroelectric material per unit volume per unit time. It is expressed in W/L and defined as follows:

$$P_D = f N_D \quad (13)$$

where  $f$  is the overall cycle frequency defined as  $f = (\sum \tau_{ij})^{-1}$ , where  $\tau_{ij}$  is the duration of process  $i$ - $j$ . Note that  $N_D$  is also dependent on the cycle frequency.<sup>129,131</sup>

Overall, desirable properties in pyroelectric materials to maximize electrical energy and power densities include (i) large dielectric strength to enable the application of large electric fields without breakdown, (ii) small leakage current caused by electrical conduction

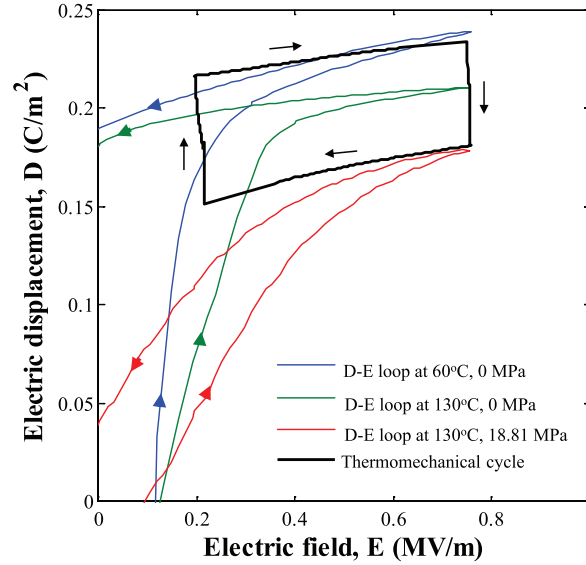


**FIG. 16:** Isothermal bipolar D-E loops of PMN-28PT and experimental thermomechanical power cycle performed at frequency  $f = 0.025$  Hz with (i) electric field ranging between  $E_L = 0.2$  MV/m and  $E_H = 0.75$  MV/m, (ii) temperatures between  $T_{cold} = 52^\circ\text{C}$  and  $T_{hot} = 109^\circ\text{C}$ , and (iii) compressive stress  $\sigma_H = 18.81$  MPa. Here, the energy density  $N_D$  was 33.6 J/L/cycle.

through the material that reduces the energy density, (iii) short discharge time of the surface charges in order to minimize cycle period, maximize frequency and power density, and (iv) small thermal inertia to enable rapid isoelectric heating and cooling processes to maximize power density. Note also that the energy and power densities do not reach their respective maximum at the same frequency.<sup>30</sup> Indeed, low frequency ensures that the PE has time to reach the cold and hot source temperatures (i.e.,  $T_{cold} = T_C$  and  $T_{hot} = T_H$ ). Then, the processes can be considered as a series of quasi-equilibrium states and the energy density reaches its maximum  $N_{D,max}$ . Increasing the frequency may be beneficial to increasing the power density. However, it tends to reduce the temperature swing of the PE, particularly if the latter has large thermal mass. Typically, the power density  $P_D$  increases with increasing cycle frequency to reach a maximum  $P_{D,max}$  a critical frequency beyond which it decreases.<sup>30,126</sup>

Moreover, the pyroelectric material efficiency of a power cycle is defined as the ratio of the electrical energy generated to the thermal and/or mechanical energy consumed during the cycle. The thermomechanical cycle converts both thermal and mechanical energies into electrical energy. Then, the material efficiency  $\eta_m$  can be expressed as

$$\eta_m = \frac{N_D}{Q_{in} + W_{in}} \quad (14)$$

Note that this definition of efficiency is consistent with that used for piezoelectric materials given by  $\eta_m = N_D/W_{in}$  (Ref. 132) and for the Olsen cycle given by  $\eta_m = N_D/Q_{in}$ .<sup>118</sup>

The thermal energy density  $Q_{in}$  provided per unit volume of pyroelectric material during the cycle may be expressed as

$$Q_{in} = \oint \rho c_p(T) dT \quad (15)$$

The specific heat  $c_p(T)$  is temperature-dependent and accounts for phase transition, as illustrated in Fig. 9(b). Similarly, the net mechanical work  $W_{in}$  provided during the cycle per unit volume of pyroelectric material can be defined as

$$W_{in} = \oint \sigma(\epsilon) d\epsilon \quad (16)$$

where  $\epsilon$  represents the strain in the direction parallel to the polarization. For ferroelectric materials undergoing phase transition(s), the relationship between  $\sigma$  and  $\epsilon$  is typically nonlinear.<sup>46,66</sup> Thus,  $W_{in}$  cannot be expressed in terms of the Young's modulus. Instead, it should be estimated from actual stress-strain curves.<sup>133</sup>

Finally, the material efficiency  $\eta_m$  defined above accounts for the conversion of thermomechanical energy into electricity by the material alone. However, it does not represent the efficiency of a potential device implementing the cycle. The latter may require additional heat and work input to operate and is also subject to heat losses, friction, and other irreversible processes. In other words,  $\eta_m$  represents the upper limit of efficiency achievable by a pyroelectric energy converter using the material and cycle under consideration.

## 4. OLSEN CYCLE

Of all the pyroelectric energy conversion cycles introduced in Section 3.2, the Olsen cycle has been the most studied due to the fact that it has achieved the largest demonstrated energy<sup>60</sup> and power<sup>120</sup> densities per unit volume of material among the different pyroelectric energy conversion methods.

### 4.1 Practical Implementation

Typical experimental methods and devices implementing the Olsen cycle consist of an electrical and a thermal subsystem as described in the following sections.

#### 4.1.1 Electrical Subsystem

The electrical subsystem serves two main purposes (i) to control the electric field applied to the pyroelectric element and impose  $E_L$  or  $E_H$  at appropriate time during the Olsen cycle (see Fig. 13), and (ii) to determine, and potentially store, the energy and power generated by the pyroelectric element by measuring the voltage  $V$  and charges  $Q$  displayed by the pyroelectric element. Figure 17 shows a modified Sawyer-Tower circuit<sup>19,134</sup> typically used for measuring D-E loops and the energy generated by the Olsen cycle.<sup>29,81,113,116,125–129,135</sup>

A resistive voltage divider is placed in parallel with the Sawyer-Tower bridge to control the electric field imposed on the pyroelectric element. Voltage  $V_1$  across the film capacitor can be measured using an electrometer, featuring a very large internal resistance in order to minimize discharge of the capacitor  $C_1$  in series with the PE. The resistor  $R_L$  acts as

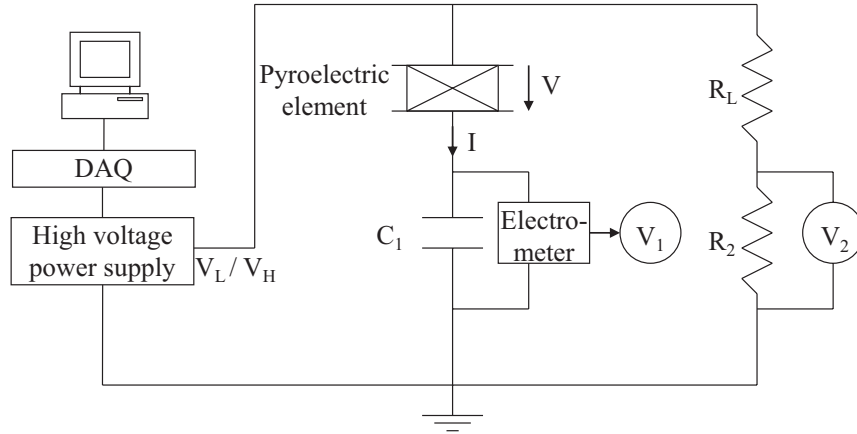


**FIG. 17:** Typical electric circuit used to perform pyroelectric energy conversion cycles (adapted from Navid and Pilon, 2011, Nguyen et al., 2010, Lee et al., 2013, and Olsen et al., 1985).<sup>29,30,60,81</sup>

a voltage divider to scale down the voltage across the resistor  $R_2$  in order to not exceed the maximum voltage input of the data acquisition system (DAQ). The electric field can be applied by a computer-generated function through the DAQ connected to a high-voltage power supply. The magnitude of the film electric displacement  $D$  is determined from

$$D = \frac{Q}{A} = \frac{C_1 V_1}{A} \quad (17)$$

where  $A$  is the pyroelectric film's surface area (Fig. 3). The magnitude of the electric field across the PE can be calculated from Ohm's law and Kirchhoff's law and expressed as follows:

$$E = \frac{V}{b} = \frac{V_2(1 + R_L/R_2) - V_1}{b} \quad (18)$$

where  $b$  is the pyroelectric film thickness (Fig. 3). Then, the Olsen cycle can be represented in the D-E diagram using estimates of  $D$  and  $E$  from Eqs. (17) and (18).

#### 4.1.2 Thermal Subsystem

The thermal subsystem depends on the heat source and on the heat transfer mode used for cooling and heating the pyroelectric element between  $T_{cold}$  and  $T_{hot}$  during the Olsen cycle. Conduction, convection, and radiation are the three possible modes of heat transfer. In all cases, the thermal subsystem consists of a cold and a hot source maintained at temperatures  $T_C$  and  $T_H$ , respectively. Note that these temperatures may differ from the cold and hot temperatures  $T_{cold}$  and  $T_{hot}$ , reached by the pyroelectric element during the cycle.

##### 4.1.2.1 Dipping Experiments

A simple method for implementing the Olsen cycle is to successively dip the PE in hot and cold baths of dielectric fluid(s) maintained at temperatures  $T_C$  and  $T_H$  while imposing

the desired electric field.<sup>29,79,83,85,125</sup> This so-called dipping experiment is very simple to implement and can be used to assess the maximum amount of energy and power generated by a pyroelectric material under somehow idealized conditions. Indeed, this method avoids dealing with challenges associated with heat transfer limitations, heat losses, and assembly encountered in actual devices. This method has been used extensively for the screening of promising pyroelectric materials, including nonporous or porous P(VDF-TrFE),<sup>29,79,83</sup> PMN-*x*PT,<sup>127,128</sup> PZN-PT,<sup>129</sup> and PLZT.<sup>60,125</sup>

#### 4.1.2.2 Heat Conduction

Heat conduction can be used to heat up and cool down the pyroelectric element in the Olsen cycle through a stamping procedure illustrated in Fig. 18.<sup>136</sup> It consists of alternately pressing a pyroelectric element in thermal contact with cold and hot blocks respectively kept at temperature  $T_C$  and  $T_H$  while imposing an electric field across the pyroelectric element as prescribed by the Olsen cycle. Lee et al.<sup>136</sup> used 50  $\mu\text{m}$  thick co-polymer 60/40 P(VDF-TrFE) films as the pyroelectric material supported by a wooden stamp.

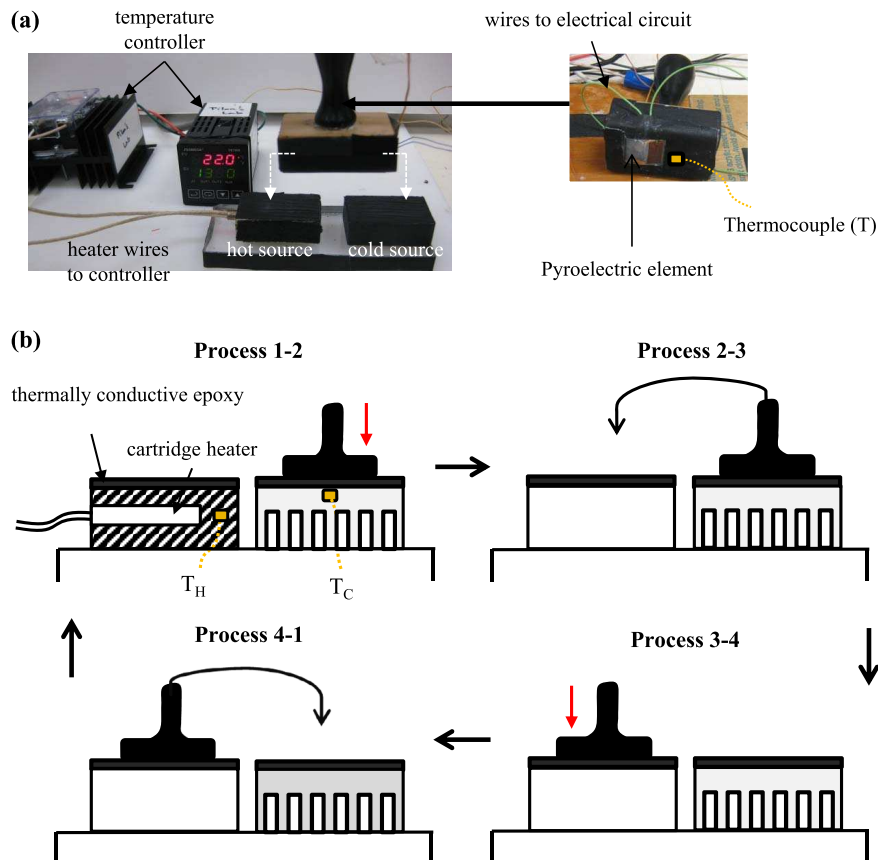


**FIG. 18:** (a) Photographs of the thermal subsystem used to create periodic temperature oscillations by the stamping procedure as well as of the PE-stamp assembly and (b) schematic of the associated implementation of the Olsen cycle (adapted from Lee et al., 2010).<sup>136</sup>

blocks either heated with a cartridge heater or cooled by natural convection thanks to a finned heat sink were used as the hot and cold sources, respectively. They were coated with a thermally conductive but electrically insulating epoxy film so that the pyroelectric element was in thermal contact but not in electrical contact with the hot and cold sources. The authors reported a maximum energy density of 155 J/L/cycle at 0.066 Hz for temperatures  $T_C$  and  $T_H$  of 25 and 110°C electric fields between 20 and 35 MV/m.

Moreover, Cha and Ju<sup>126</sup> demonstrated the Olsen cycle up to 0.8 Hz on 56/44 P(VDF-TrFE) by taking advantage of liquid-based switchable thermal interfaces to provide heating and cooling. This liquid interface presents the advantage of reducing contact resistance between the PE and the cold and hot sources. The authors reported a maximum energy density of 250 J/L/cycle at 0.25 Hz and power density of 110 W/L around 1 Hz for temperatures  $T_C$  and  $T_H$  of 40 and 100°C electric fields between 20 and 35 MV/m.

#### 4.1.2.3 Forced Convection

Compared to heat conduction, convective heat transfer is arguably a faster way to heat up and cool down the pyroelectric element. In the context of the Olsen cycle, it can be implemented by alternatively flowing hot and cold dielectric working fluid over one face of a pyroelectric element, as performed by Ikura<sup>13</sup> on P(VDF-TrFE) films. However, the power output and efficiency of such a pyroelectric converter can be significantly improved by using (i) heat regeneration<sup>113</sup> and (ii) multistaging.<sup>117</sup>

*Heat regeneration* consists of oscillating a working fluid over one or both faces of the PE located between the hot and cold sources. The fluid flow should be laminar in order to preserve the temperature gradient between the hot and the cold sources. Heat regeneration can significantly reduce heat losses from the system by cycling the heat back and forth between the pyroelectric element and the working fluid. It has been established theoretically that pyroelectric conversion cycles based on heat regeneration using an oscillating working fluid and the Olsen cycle can reach Carnot efficiency between a hot and a cold thermal reservoir.<sup>33</sup> However, in practice, limitations in reaching Carnot efficiency include (i) leakage current, (ii) heat losses to the surrounding, and (iii) sensible (thermal) energy required to heat the material. Heat regeneration has been successfully implemented experimentally.<sup>30,113</sup>

*Multistaging* refers to the placement of different pyroelectric materials with increasing Curie temperature from the cold to the hot sources along the oscillating temperature gradient. A large fraction of the power is generated during phase transition, and in particular ferroelectric to paraelectric at  $T_{Curie}$ .<sup>86,128</sup> Thus, the pyroelectric material at a given location should be chosen such that its  $T_{Curie}$  falls within the range of the local temperature oscillations, resulting in more efficient power generation. Multistaging has been demonstrated by Olsen et al.<sup>117</sup>

#### 4.1.2.4 Radiation

Heat conduction and convective heat transfer under laminar flow are inherently slow and limit the operating frequency of the Olsen cycle and therefore the power density. By contrast, radiative heat transfer takes place at the speed of light. Thus, a pyroelectric material

can reach its phase transition temperature rapidly during the Olsen cycle when heated by radiation. In fact, radiation has been used as a heat source to heat up pyroelectric elements.<sup>91,95,102</sup> Planck's blackbody radiation theory imposes a limit on the maximum radiative transfer between two surfaces at given temperatures. It applies in the far field when the gap size  $d$  separating radiating surfaces is much larger than the peak radiation wavelength ( $d \gg \lambda_{max}$ ).<sup>137</sup> According to Wien's displacement law ( $\lambda_{max}T = 2898 \mu\text{m}\cdot\text{K}$ ), the peak radiation wavelength  $\lambda_{max}$  is around  $10 \mu\text{m}$  for the temperature range between  $\sim 300$  and  $400 \text{ K}$ . In the far field, temporal temperature oscillation in the PE can be achieved by exposing it to a thermal radiation source (e.g., heat lamp or sunlight) periodically obstructed by a chopper<sup>91,95,102</sup> as performed in motion sensors and infrared detectors.<sup>12</sup>

For gap sizes much smaller or comparable to the peak wavelength ( $d \ll \lambda_{max}$ ), thermal radiation can be increased by several orders of magnitude by varying the subwavelength distance between the PE and the cold and hot sources.<sup>138</sup> The thermal radiation enhancement in the near field is attributed to evanescent waves tunneling through the small gap.<sup>137,139</sup> These nonpropagating waves only transport energy when an object is brought in close proximity to an emitter. In the case of dielectric materials, surface waves called surface phonon polaritons are excited by infrared radiation due to coupling between the electromagnetic field and optical phonons.<sup>138</sup> Thus, temporal temperature oscillations can be achieved by periodically bringing the PE in close proximity with the cold and hot sources.<sup>140,141</sup> Fang et al.<sup>140</sup> performed numerical simulations of a pyroelectric converter harvesting nanoscale thermal radiation using 60/40 P(VDF-TrFE) and PMN-10PT. The converter consisted of a composite pyroelectric plate oscillating between hot and cold plates separated by a nanosized gap.<sup>140</sup> Each of these plates consisted of an aluminum plate coated with a  $1 \mu\text{m}$  thick  $\text{SiO}_2$  absorbing layer. Similarly, the PE plate consisted of a ferroelectric composite thin film coated with  $\text{SiO}_2$ . This was meant to further enhance radiative heat fluxes as silicon dioxide  $\text{SiO}_2$  is a dielectric material exhibiting large absorption index at wavelengths of  $\sim 10 \mu\text{m}$ . Note that, in these simulations, the device was assumed to operate under vacuum to minimize friction on the oscillating PE plate and to reduce heat losses to the surrounding. The concept of multistaging can also be applied with this mode of heat transfer by superimposing pyroelectric films with different compositions and Curie temperature and separated by electrodes. The simulations showed that for a multilayer composite PMN-10PT thin film, an efficiency of 1.35% and a power output of  $6.5 \text{ mW/cm}^2$  was predicted for cold and hot plates at  $10$  and  $110^\circ\text{C}$ .<sup>140</sup> The simulated operating frequency was  $1.2 \text{ Hz}$ , more than 10 times greater than that of actual devices employing laminar convective heat transfer.<sup>29,30,140</sup> A similar concept has been explored for converting spacecraft waste heat into electricity.<sup>142</sup> In practice, however, maintaining a nanoscale gap ( $\sim 100 \text{ nm}$  or less) between the PE and the hot or cold plates remains challenging.

## 4.2 Performance Comparisons

Numerous studies have investigated the Olsen cycle performed on ferroelectric polymers P(VDF-TrFE),<sup>29,30,33,79,136</sup> single crystals PMN-PT and PZN-PT,<sup>127-129</sup> and PLZT ceramics.<sup>106,113-115,117,125,143</sup> The following sections compare the performance of these materials in terms of energy and power densities.

### 4.2.1 Maximum Energy Density

Table 3 compares the maximum energy density  $N_{D,max}$  generated experimentally by performing the Olsen cycle on various materials for different temperatures  $T_C$  and  $T_H$ , and operating electric fields  $E_L$  and  $E_H$ . These measurements were performed at low frequency under quasi-equilibrium conditions implying  $T_C = T_{cold}$  and  $T_H = T_{hot}$ . The latter refer to operations when the electric displacement reached a steady state during isoelectric field heating (process 2–3) and cooling (process 4–1) before the electric field was varied to perform processes 3–4 and 1–2, respectively. Most of the results reported in Table 3 were obtained using dipping experiments.

Single crystals PMN- $x$ PT and PZN- $x$ PT produced energy density on the order of 100–200 J/L/cycle.<sup>118,127,129,144</sup> This is significantly less than that produced by PLZT ceramics and by some P(VDF-TrFE). However, single crystals are useful model materials to understand the material behavior and phase transitions occurring during the Olsen cycle.<sup>128</sup> Note that a maximum energy density of 900 J/L/cycle was reported by Olsen et al.<sup>83</sup> for 60/40 P(VDF-TrFE) films with temperatures  $T_C$  and  $T_H$  of 25°C and 120°C and electric

**TABLE 3:** Comparison of the maximum energy density  $N_{D,max}$  achieved experimentally by different materials subjected to the Olsen cycle at low frequency along with temperature and electric field ranges

Material	$T_C$ (°C)	$T_H$ (°C)	$E_L$ (MV/m)	$E_H$ (MV/m)	$N_{D,max}$ (J/L/cycle)	Refs.
PZST	157	177	0.4	3.2	131	117
PZST	145	178	1.2	3.2	130	113
PZST	146	159	0.0	2.9	100	81
PZST	110	170	0.0	2.8	0.4	115
73/27 P(VDF-TrFE)	23	67	23.0	53.0	30	33
60/40 P(VDF-TrFE)	25	120	20.0	60.0	900	83
60/40 P(VDF-TrFE)	58	77	4.1	47.2	52	13
60/40 P(VDF-TrFE)	50	100	6.23	27.6	165	79
60/40 P(VDF-TrFE)	67	81	20.3	37.9	130	30
60/40 P(VDF-TrFE)	25	110	20.0	50.0	521	29
61.3/29.7/9 P(VDF-TrFE-CFE)	0	25	0.0	25.0	50	166
PZN-4.5PT	100	160	0.0	2.0	217	144
PZN-5.5PT	100	190	0.0	1.2	150	129
PMN-10PT	30	80	0.0	3.5	186	118
PMN-28PT	90	170	0.2	0.75	86	130
PMN-32PT	180	170	0.0	0.9	100	127
5/65/35 PLZT	40	250	0.4	7.5	799	60
6/65/35 PLZT	40	210	0.4	8.5	949	60
7/65/35 PLZT	30	200	0.2	7.0	1013	60
8/65/35 PLZT	25	160	0.2	7.5	888	125
9/65/35 PLZT	3	150	0.4	7.5	653	60
9.5/65/35 PLZT	3	140	0.2	6.0	637	135

field cycled between  $E_L = 20$  and  $E_H = 60$  MV/m. However, it is unclear whether these experimental results were averaged over multiple cycles and if they were repeatable. In fact, Navid et al.<sup>29</sup> produced 521 J/L/cycle averaged over five cycles for the same material, temperature range, and operating electric fields.

To the best of our knowledge, the maximum energy density  $N_{D,max}$  was reported at 1013 J/L/cycle for 7/65/35 PLZT.<sup>60</sup> Figure 19 presents the corresponding Olsen cycles in the D-E diagram with PE temperature oscillating between  $T_C = T_{cold} = 30^\circ\text{C}$  and  $T_H = T_{hot} = 200^\circ\text{C}$  and electric field between  $E_L = 0.2$  MV/m and  $E_H = 7.0$  MV/m.<sup>60</sup> Note also that the D-E paths of the Olsen cycles were not perfectly closed since points 4 and 4' did not coincide. The offset between points 4' and 4 can be explained by the leakage current observed across the PLZT ceramic at high temperatures and/or large electric fields.<sup>29,33,85,86</sup> In addition, the Olsen cycles did not follow a smooth path between  $E_L$  and  $E_H$  during isothermal processes 1–2 and 3–4. This was likely due to microcracks propagating along the grain boundaries of the sample while the Olsen cycle was performed.<sup>145</sup> These fractures introduced spatial variations in the local electric field near the crack front, resulting in sample inhomogeneity.<sup>146</sup> Finally, this was performed at frequency of 0.0256 Hz corresponding to power density of 25.9 W/L. Despite the low frequency, the power density was much larger than the largest power density of 1.08 W/L (Ref. 101) reported for linear pyroelectric energy conversion (see Table 2).

#### 4.2.2 Maximum Power Density

Table 4 summarizes the maximum power density  $P_{D,max}$  achieved experimentally to date and reported in the literature along with the associated operating parameters  $T_C$ ,  $T_H$ ,  $E_L$ ,

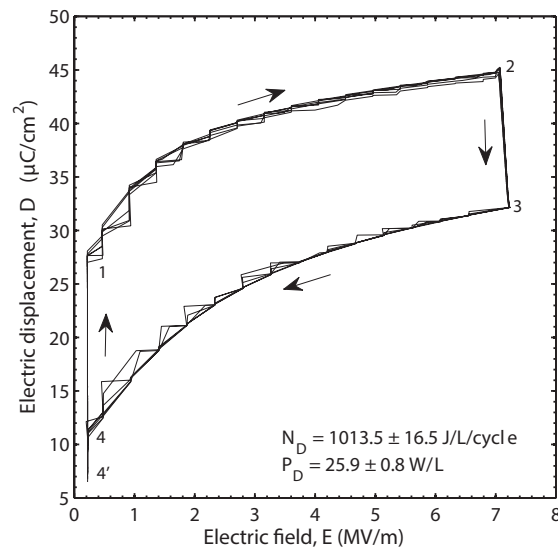


**FIG. 19:** Electric displacement  $D$  versus electric field  $E$  diagram for six consecutive Olsen cycles experimentally obtained using dipping experiments with 7/65/35 PLZT at 0.0256 Hz for  $E_L = 0.2$  MV/m,  $E_H = 7.0$  MV/m,  $T_C = 30^\circ\text{C}$ , and  $T_H = 200^\circ\text{C}$  (adapted from Lee et al., 2013).<sup>60</sup>

**TABLE 4:** Summary of maximum power density  $P_{D,max}$  experimentally obtained using the Olsen cycle or reported for different materials, temperature ranges, operating electric fields, and frequencies

Material	$T_C$ (°C)	$T_H$ (°C)	$E_L$ (MV/m)	$E_H$ (MV/m)	$f$ (Hz)	$P_{D,max}$ (W/L)	Refs.
BaTiO <sub>3</sub>	20	130	0.183	0.2	1000	3000	120
PZST	156.8	177.4	0.4	2.8	0.26	33.9	117
73/27 P(VDF-TrFE)	23.0	67.0	23.0	53.0	0.079	2.38	33
60/40 P(VDF-TrFE)	25.0	120.0	20.0	50.0	0.125	112.5	83
60/40 P(VDF-TrFE)	58.3	76.5	4.0	48.0	0.256	13.3	13
60/40 P(VDF-TrFE)	67.3	81.4	20.2	37.9	0.12	10.7	30
60/40 P(VDF-TrFE)	25.0	120.0	20.0	50.0	0.13	58.0	29
56/44 P(VDF-TrFE)	40	100	5	50	0.6	110	126
PZN-4.5PT	100.0	160.0	0.0	1.0	0.10	24.4	144
PZN-5.5PT	100.0	190.0	0.0	1.5	0.10	11.7	129
PMN-32PT	80.0	170.0	0.2	0.9	0.049	4.92	127
5/65/35 PLZT	40.0	250.0	0.4	9.0	0.066	41.8	60
6/65/35 PLZT	40.0	210.0	0.0	8.5	0.060	47.9	60
7/65/35 PLZT	30.0	200.0	0.0	8.5	0.084	47.5	60
8/65/35 PLZT	25.0	160.0	0.2	9.0	0.063	39.5	60
9/65/35 PLZT	3.0	150.0	0.2	7.0	0.071	35.9	60
9.5/65/35 PLZT	3.0	140.0	0.2	6.0	0.125	55.3	135

$E_H$ , and  $f$ . Note that many of these data were obtained at low frequency with the goal of maximizing the energy density (Table 3) but not necessarily the power density. They are nonetheless presented in Table 4 as a reference. Olsen et al.<sup>83</sup> performed dipping experiments on 60/40 P(VDF-TrFE) films and reported a power density of 112.5 W/L corresponding to the case of energy density of 900 J/L/cycle previously discussed. Ikura<sup>13</sup> reported a power density of 13.3 W/L for 60/40 P(VDF-TrFE) subjected to dipping experiments at 0.256 Hz with  $T_{cold} = 58^\circ\text{C}$  and  $T_{hot} = 76^\circ\text{C}$  while the electric field was cycled between 4 and 48 MV/m. Khodayari et al.<sup>144</sup> performed the Olsen (or Ericsson) cycle on [110]-poled single crystal PZN-4.5PT and generated 24.4 W/L at 0.1 Hz for temperature cycling between 100 and 160°C and electric field between 0 and 1.0 MV/m. Meanwhile, Navid et al.<sup>29</sup> reported a power density generated by the Olsen cycle, under quasiequilibrium conditions, of 58, 36, and 18 W/L for commercial, purified, and porous 60/40 P(VDF-TrFE) films, respectively. The 60/40 P(VDF-TrFE) films were dipped into cold and hot silicone oil baths at 25°C and 100–120°C, respectively. The low electric field was  $E_L = 20$  MV/m and the high electric field  $E_H$  varied between 30 and 60 MV/m.

Lee et al.<sup>125</sup> performed dipping experiments on relaxor ferroelectric  $x/65/35$  PLZT with  $x$  varying between 5 and 9 mol.%. A maximum energy density of 1013 J/L/cycle was generated at 0.084 Hz, corresponding to a power density of 47.5 W/L, for operating temperatures between 25 and 160°C and electric field cycled between 0.2 and 7.5 MV/m. Chin et al.<sup>135</sup> performed a similar procedure on 9.5/65/35 PLZT ceramics and achieved a

maximum power density of 55 W/L at 0.125 Hz. The Olsen cycle was performed between 3 and 140°C and electric field from 0.2 to 6.0 MV/m.

Bhatia et al.<sup>120</sup> successfully demonstrated a microfabricated device performing the Olsen cycle on a 150 nm thick BaTiO<sub>3</sub> film with SrRuO<sub>3</sub> electrodes at frequencies up to 1 kHz. The pyroelectric film was heated by heat conduction from a resistive heater consisting of a gold strip deposited on top of the pyroelectric element and subjected to a high-frequency sinusoidal voltage. The Olsen cycle was performed below the Curie temperature  $T_{Curie}$  of BaTiO<sub>3</sub> estimated to be  $\sim 400^\circ\text{C}$ . Bhatia et al.<sup>120</sup> investigated the effect of the phase difference and amplitude of time rate of change of temperature and electric field on the generated power density. They achieved a maximum power density of 3000 W/L; the largest reported to date. However, the energy density was only 3–4 J/L/cycle. This points to the need of optimizing the pyroelectric material choice and dimensions as well as the operating frequency to achieve the desired range of energy and power densities.

Finally, comparing Tables 2–4 establishes that the Olsen pyroelectric energy conversion cycle produces both the largest electrical energy<sup>60</sup> and power<sup>120</sup> per unit volume of material among the different pyroelectric energy conversion methods. In fact,  $N_{D,max}$  exceeded 1000 J/L/cycle for Olsen cycle on 7/65/35 PLZT<sup>60</sup> compared to 30 J/L/cycle for linear pyroelectric energy conversion with PZT.<sup>99</sup> Similarly,  $P_{D,max}$  was  $\sim 3000$  W/L with BaTiO<sub>3</sub> thin films<sup>120</sup> compared to 1.08 W/L for linear pyroelectric energy conversion with PVDF.<sup>101</sup>

#### 4.2.3 Comparison with Thermomechanical Cycle

Table 5 compares the operating conditions, the energy inputs  $Q_{in}$  and  $W_{in}$ , the energy density  $N_D$ , and the material efficiency  $\eta_m$  obtained experimentally with the Olsen cycle and the thermomechanical cycle both performed on PMN-28PT. The material efficiency  $\eta_m$  of the cycles was estimated using Eq. (14). The thermal energy  $Q_{in}$  was estimated according

**TABLE 5:** List of operating conditions, energy inputs  $Q_{in}$  and  $W_{in}$ , generated energy density  $N_D$ , and material efficiency  $\eta_m$  for the thermomechanical (TM) and the Olsen cycles. In all cases, the low electric field was  $E_L = 0.2$  MV/m

Cycle type	$f$ (Hz)	$E_H$ (MV/m)	$T_H$ (°C)	$T_{hot}$ (°C)	$T_{cold}$ (°C)	$\sigma_H$ (MPa)	$W_{in}$ (J/L)	$Q_{in}$ (J/L)	$N_D$ (J/L)	$\eta_m$ (%)
Olsen	0.021	0.75	170	170	90	0	0	540	86	15.9
TM	0.025	0.75	157	108.5	51.9	18.81	30	1202	24	2.0
TM	0.025	0.75	107	73.9	40.2	18.81	30	292	15	4.7
TM	0.125	0.75	160	103.1	90.4	25.13	41	301	32	9.4
TM	0.125	0.75	130	85.1	74.4	25.13	41	469	31	6.1
TM	0.5	0.75	160	100.9	99.9	25.13	41	21	27	43.5
TM	0.5	0.75	130	83.2	82.2	25.13	41	62	26	25.2
TM	1	0.75	160	104.4	104.3	25.13	41	2	26	60.5
TM	1	0.75	130	85.4	85.3	25.13	41	9	25	50.0
TM	1	0.95	130	85.4	85.3	33.56	55	9	41	64.1

to Eq. (15) using the measured specific heat  $c_p$  presented in Fig. 9(b). The mechanical energy input  $W_{in}$  was computed from Eq. (16) using the area enclosed by the stress-strain curves at 85°C measured at 0.2 and 0.95 MV/m for [001] PMN-28PT single crystals.<sup>147</sup>

First, Table 5 reports a material efficiency  $\eta_m$  of 15.9% for PMN-28PT subjected to the Olsen cycle at low frequency between  $T_C = 22^\circ\text{C}$  and  $T_H = 170^\circ\text{C}$  and  $E_H = 0.75$  MV/m. This represents 48% of the Carnot efficiency. Moreover, the thermomechanical cycle at low frequency featured low material efficiency due to the large heat input. For this cycle, it was beneficial to operate at high frequency under small temperature swings and heat input to improve the cycle efficiency. For a given temperature swing, the efficiency was highly dependent on the operating temperatures. For example, the two cycles performed at 0.5 Hz resulted in similar energy density  $N_D$  and  $W_{in}$  with a temperature swing of  $T_{hot} - T_{cold} = 1^\circ\text{C}$ . However, their efficiencies differed by nearly a factor of 2. One cycle was performed between 82.3 and 83.2°C, where  $c_p(T)$  exhibited a phase transition peak and a large thermal hysteresis (9b) while the other was performed between 99.9 and 100.9°C, where no phase transition occurred. This emphasizes the importance of matching the material to the operating temperatures such that the heat input is minimized and the generated energy density is maximized in order to maximize the material efficiency  $\eta_m$ . Note, however, that the operating conditions for maximum efficiency do not necessarily coincide with those corresponding to maximum energy or power densities. The largest material efficiency was 64% for the thermomechanical cycle performed at 1 Hz with temperature  $\sim 85^\circ\text{C}$  near the Curie temperature. In this case, the heat input was  $Q_{in} = 9$  kJ/m<sup>3</sup> and the mechanical work performed was  $W_{in} = 55$  kJ/m<sup>3</sup>.

#### 4.2.4 Physical Modeling

Kandilian et al.<sup>127</sup> developed a physical model predicting the amount of energy generated by ferroelectric materials undergoing the Olsen cycle. The model accounted for temperature-dependent properties of the material and assumed a linear relationship between electric displacement and electric field at high fields given by Eq. (9). The energy density  $N_D$  was expressed as follows:<sup>127</sup>

$$N_D(T_{cold}, T_{hot}, E_L, E_H) = (E_H - E_L) \left\{ \frac{\epsilon_0}{2} [\epsilon_{r,H}(T_{cold}) - \epsilon_{r,H}(T_{hot})] (E_H + E_L) + P_{sat}(T_{cold}) - P_{sat}(T_{hot}) + \frac{d_{33}x_3}{s_{33}} \right\} \quad (19)$$

where  $\epsilon_{r,H}(T_{cold})$  and  $\epsilon_{r,H}(T_{hot})$  refer to the relative permittivity of the pyroelectric material at low frequency under high electric field at the cold and hot temperatures  $T_{cold}$  and  $T_{hot}$  reached by the PE, respectively (Fig. 13). The saturation polarizations at  $T_{cold}$  and  $T_{hot}$  are denoted by  $P_{sat}(T_{cold})$  and  $P_{sat}(T_{hot})$ , respectively. The last term on the right-hand side of Eq. (19) represents the contribution of the secondary pyroelectric coefficient to the generated energy density due to dimensional changes in the crystal structure caused by temperature changes.<sup>148</sup> The piezoelectric coefficient is  $d_{33}$ ,  $s_{33}$  is the elastic compliance, and  $x_3 = \int_{T_C}^T \alpha_3(T) dT$ , where  $\alpha_3(T)$  is the linear thermal expansion coefficient.<sup>128</sup>

Note that this model was based on the assumption that the dielectric contribution to the primary pyroelectric coefficient was negligible compared with the dipole contribution, see Eq. (8) in Ref. 127.

This model was first validated against experimental data collected on PMN-32PT single crystal.<sup>127</sup> using  $\epsilon_{r,H}(T)$  and  $P_{sat}(T)$  reported in Ref. 23. Figure 20(a) shows the Olsen cycle performed on PMN-32PT at low frequency along with the isothermal bipolar D-E loops at  $T_C = 80^\circ\text{C}$  and  $T_H = 140^\circ\text{C}$ . It is evident that the Olsen cycle exceeded the bounds of the isothermal D-E loops at the silicone oil bath temperatures  $T_C$  and  $T_H$ . This was attributed to the secondary pyroelectric effect occurring during the heating process 3–4 featuring a rhombohedral to tetragonal phase transition and accounted for by the last term of Eq. (19).<sup>127</sup> In fact, Fig. 20(b) illustrates the relatively good agreement obtained between experimental results and model predictions for different values of electric field  $E_H$ .<sup>127</sup> This model has also been validated against the energy density experimentally measured with PZN-5.5PT,<sup>129</sup> PMN-28PT,<sup>128</sup> 8/65/35 PLZT ceramics,<sup>125</sup> as well as P(VDF-TrFE)<sup>126</sup> for a wide range of electric fields and temperatures. In these cases, however, the contribution from the secondary pyroelectric effect was ignored because the Olsen cycle fell within the bounds of the isothermal D-E loops at  $T_C$  and  $T_H$ .

Finally, note that a large number of recent studies have theoretically predicted the energy and power densities from the Olsen cycle for a wide range of materials by computing the area between isothermal bipolar D-E loops measured or reported in the literature at various temperatures.<sup>124,149–156</sup> In other words, these authors did not implement the Olsen cycle experimentally. This approach is questionable on multiple counts. First, conceptually, Figs. 16 and 20(a) show that, in practice, the Olsen cycle does not always precisely follow the isothermal bipolar D-E loops even when they are measured at the same frequency as the cycle. Second, reported experimental isothermal D-E loops were limited to a few temperatures and frequencies. Thus, computing  $N_D$  and  $P_D$  for arbitrary values of  $T_C$ ,  $T_H$ ,  $E_L$ ,  $E_H$ , and  $f$  does not guarantee that the pyroelectric element will reach temperatures for

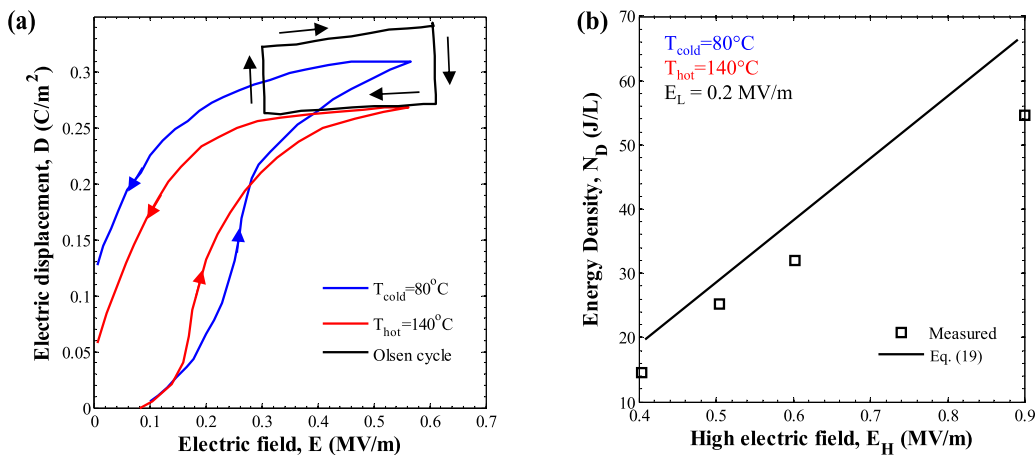


**FIG. 20:** (a) Experimentally measured D-E loops and Olsen cycle performed on PMN-32PT single crystals and (b) energy density generated versus high electric field  $E_H$  for  $T_C = 80^\circ\text{C}$ ,  $T_H = 140^\circ\text{C}$ , and  $E_L = 0.2$  MV/m (adapted from Kandilian et al., 2011).<sup>127</sup>

which D-E loops are available. Third, the D-E loops depend on frequency particularly at frequencies above 1 Hz.<sup>157</sup> Thus, predictions varying the frequency should ensure that the appropriate D-E loops are available. In addition, from a practical point of view, experimental implementation is limited by (i) the magnitude of repeated temperature and electric field changes that can be imposed on the PE without causing cracking and electric breakdown, (ii) leakage current that is not accounted for by models or by computing the area between D-E loops, and (iii) thermal inertia of the pyroelectric element that limits the operating frequency. In fact, the duration of the heating and cooling processes typically dominate the duration of the cycle.<sup>129,135</sup> Therefore, while estimated  $N_D$  and  $P_D$  from the D-E loops may constitute a quick way to screen for promising materials, one must be realistic in the choices of operating conditions for repeated cycling. Until these results are confirmed experimentally, we recommend that the reported estimates of energy and power densities be taken with caution.

### 4.3 Olsen Pyroelectric Converters

#### 4.3.1 Device Efficiency

Previous discussion of performance has focused on materials irrespective of the practical implementation of the cycle into an actual device. In order to assess the performance of the pyroelectric converter based on the Olsen cycle, the thermodynamic energy efficiency of the device  $\eta_d$  over a cycle is defined as follows:<sup>158</sup>

$$\eta_d = \frac{\dot{W}_{net}}{\dot{Q}_{in}} \quad (20)$$

where  $\dot{Q}_{in}$  is the total heat transfer rate provided to the converter during one cycle and  $P_{net}$  is the net power produced by the device. The latter is equal to total electrical power generated during the cycle  $\dot{W}_e$ , minus any power  $\dot{W}_c$  consumed to perform the cycle in the specific device considered (i.e.,  $\dot{W}_{net} = \dot{W}_e - \dot{W}_c$ ). As an example, consider a regenerative pyroelectric energy converter using oscillatory convective heat transfer to heat up and cool down the PE.<sup>117</sup> Such device uses of a piston to achieve oscillatory flow of the working fluid thus, requiring power to pump the fluid and to overcome frictions and other irreversible processes.

#### 4.3.2 Prototypical Devices

To the best of our knowledge, only seven prototypical pyroelectric converters based on the Olsen cycle using regeneration have been built to date. Table 6 summarizes the material, working fluid, frequency, cold and hot source temperatures, low and high electric fields, and performance of these pyroelectric converters. First, several prototypical pyroelectric energy converters implementing the Olsen cycle were designed and built by Olsen and co-workers in the 1980s.<sup>113–115,117</sup> They assembled the first regenerative devices using 250  $\mu\text{m}$  thick lead zirconate stannate titanate (PZST) as the pyroelectric materials and silicone oil as the working fluids. A piston was used to vertically oscillate the working

**TABLE 6:** Summary of design and performances of pyroelectric energy conversion devices built to date

<b>Material</b>	<b>PE thickness (arrangement)</b>	<b>Working fluid</b>	$T_C/T_H$ (°C)	$f$ (Hz)	<b>Electrodes</b>	$V_L/V_H$ (V)	<b>Electrical output</b>	$\eta_d$ (%)	<b>Refs.</b>
PZST	250 $\mu\text{m}$ (flat stack)	Silicone oil (100cSt)	145/178	0.128	Ni (sputtered)	300/800	130	0.42	113
PZST	250 $\mu\text{m}$ (flat stack)	Silicone oil (200cSt)	110/170	0.04	Ag (fired-on)	0/700	0.36	N/A	115
PZST	250 $\mu\text{m}$ (flat stack)	Silicone oil (50cSt)	145/185	0.14	Ni (sputtered)	100/1100	1.37 W	1.05	117
PZST	250 $\mu\text{m}$ (flat stack)	Silicone oil (200cSt)	146/159	0.14	Ni (sputtered)	0/700	100	N/A	81
73/27 P(VDF-TrFE)	30-70 $\mu\text{m}$ (spiral stack)	Silicone oil (200cSt)	20/90	0.1-2	Al	200/550	30	N/A	33
60/40 P(VDF-TrFE)	25 $\mu\text{m}$ (flat film)	Water	58/77	0.256	Al	100/1200	52	N/A	13
60/40 P(VDF-TrFE)	25 $\mu\text{m}$ (flat film)	Water	N/A	N/A	N/A	150/850	279	N/A	86
60/40 P(VDF-TrFE)	50 $\mu\text{m}$ (flat stack)	Silicone oil (50cSt)	69/88	0.061	Al (e-beam evap.)	150/850	130	N/A	30

fluid back and forth between a cold and a hot source.<sup>117</sup> Ceramic stacks and nylon spacers were used to form microchannels and to ensure laminar flow of the working fluid over the pyroelectric elements.<sup>33,81,113,114,117</sup> Olsen and co-workers experimentally demonstrated 1 and 40 mW devices with efficiency  $\sim 0.4\%$ .<sup>113,114</sup> Later, Olsen et al.<sup>117</sup> demonstrated the only multistage device built to date, using PZT doped with  $\text{Ti}^{4+}$  and  $\text{Sn}^{4+}$  resulting in PEs with various Curie temperatures for a maximum power output of 33 W/L at 0.26 Hz and a maximum device efficiency  $\eta_d$  of 1.05% at 0.14 Hz. The system operated between  $T_C = 145^\circ\text{C}$  and  $T_H = 185^\circ\text{C}$ .

Moreover, because of the high cost of PZST, Olsen et al.<sup>33</sup> built a device using inexpensive 30 to 70  $\mu\text{m}$  thick 73/27 P(VDF-TrFE) films sandwiched between electrodes and rolled in a spiral stack placed into a cylindrical chamber containing silicone oil. The maximum energy density of this device was 30 J/L/cycle at 0.079 Hz, while operating at temperatures between 20 and  $90^\circ\text{C}$  and electric fields between 23 and 53 MV/m.

Ikura<sup>13</sup> built a pyroelectric converter using a single P(VDF-TrFE) film over which hot and cold water streams were alternatively flown with a period of 3.9 s. The water temperature ranged from  $T_C = 58^\circ\text{C}$  to  $T_H = 77^\circ\text{C}$  resulting in an energy density between 15 and 52 J/L/cycle. Later, using the same setup, Kouchachvili and Ikura<sup>86</sup> achieved an energy density of 279 J/L per cycle by purifying a 60/40 P(VDF-TrFE) film to reduce leakage current.<sup>13,86,87</sup> Note that the frequency, temperature range, and electrode material were not disclosed in their study.<sup>86</sup>

More recently, Nguyen et al.<sup>30</sup> assembled and operated a pyroelectric converter similar to that of Olsen et al.<sup>117</sup> using 60/40 P(VDF-TrFE). Here, however, the PE was part of the microchannel walls and both of its faces were exposed to the working fluid, as illustrated in Fig. 21. The experimental design was informed by numerical simulations.<sup>159,160</sup> The maximum energy density obtained was 130 J/L/cycle at 0.061 Hz between  $66.4$  and  $83^\circ\text{C}$  while the maximum power density was 10.7 W/L at 0.12 Hz between  $67.3$  and  $81.4^\circ\text{C}$ .<sup>30</sup> In both cases, the electric field was cycled between 20.2 and 37.9 MV/m.

### 4.3.3 Simulations

Numerical simulations of pyroelectric converter based on oscillatory convective heat transfer were first performed by Olsen et al.,<sup>161</sup> who solved the one-dimensional energy equation assuming laminar, fully developed, and oscillating fluid flow within a channel driven by a piston with variable frequency and stroke length. They assumed a parabolic fluid velocity profile across channel and adiabatic channel walls. The heat transfer rate and temperature variations of the wall were determined for different stroke length and frequencies. The numerical predictions of the heat transfer rate agreed well with the experimental results for small stroke lengths but became increasingly inaccurate for larger stroke lengths. This can be attributed to the fact that the velocity profile of the working fluid was not fully developed along the microchannels as the fluid enters the microchannels from cold and hot reservoirs. In addition, axial heat conduction takes place along the stacks between the hot and cold sources but was ignored in the simulation.

Vanderpool et al.<sup>159</sup> and Navid et al.<sup>159,160</sup> completed two-dimensional transient numerical simulations to predict local time-dependent pressure, velocity, and temperature in

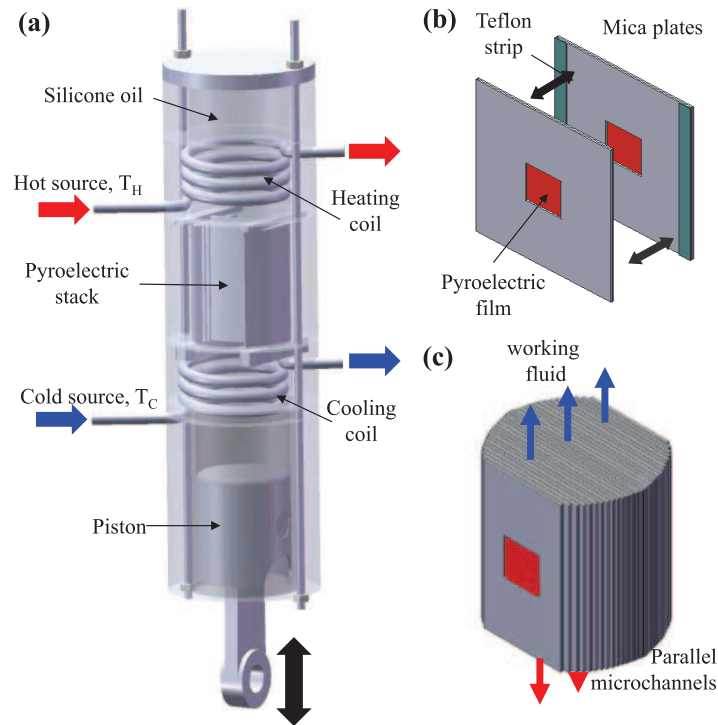


**FIG. 21:** Schematic of (a) the overall pyroelectric converter, (b) a microchannel formed by mica plates, the pyroelectric element and teflon strips, and (c) pyroelectric stack assembled by Nguyen et al. (adapted from Nguyen and Pilon, 2011, Vanderpool et al., 2008, and Navid et al., 2010).<sup>30,159,160</sup>

prototypical pyroelectric converter similar to that assembled by Olsen et al.<sup>117</sup> The objective was to identify key design and operating parameters to increase the power output and efficiency of the device. First, they established that mass, momentum, and energy equations must be solved simultaneously in order to compute the pumping power and accurately predict the temperature oscillations of the PEs. They also found that reducing the length of the device, the viscosity of the working fluid, and/or  $\rho_{c_p}$  of the pyroelectric material improved the energy efficiency and power density of the device by increasing the optimum operating frequency.<sup>160</sup> Results show that a maximum efficiency of 5.2% at 0.5 Hz could be achieved between 145 and 185°C using PZST and commercial 1.5 cst silicone oil as the working fluid with power density of 38.4 W/L. These results were confirmed by Moreno et al.,<sup>162</sup> who also validated the numerical simulation tools using experimental data collected on a pyroelectric prototype.<sup>30</sup>

#### 4.4 Challenges and Improvements

Leakage current has often been incriminated for reducing the performance of pyroelectric materials used as power generators.<sup>13,33,79,86</sup> The presence of leakage current can be identified experimentally by plotting the cycle in the D-E diagram. Figure 22(a) shows a typical

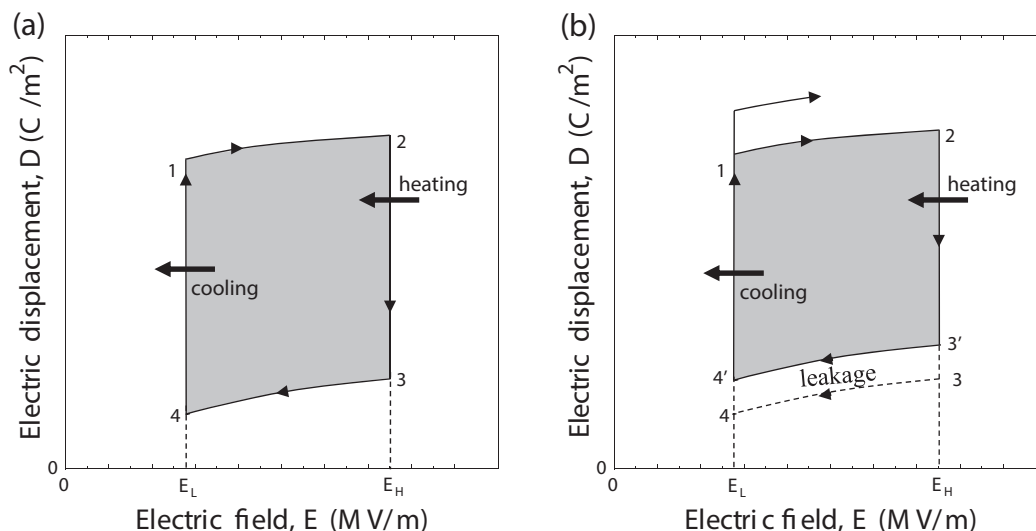


**FIG. 22:** Pyroelectric conversion cycle for a pyroelectric element (a) in absence and (b) in presence of a leakage current.

Olsen cycle for a pyroelectric element with no leakage current [i.e.,  $R = \infty$  (see Fig. 13)] and Fig. 22(b) shows one with leakage current, (i.e., finite  $R$ ). Note that, in Fig. 22(a), the cycle starts and ends at the same point and follow the same path as preceding cycles. On the other hand, in Fig. 22(b) the charge across the PE increases over time and thus the electric displacement  $D$  drifts due to leakage current. This decreases the size of the enclosed area and the generated energy per cycle. Therefore, in order to efficiently convert thermal energy into electrical energy, the leakage current must be reduced. This can be achieved by reducing the operating temperature  $T_{hot}$  and the high electric field  $E_H$ . Although this results in lower energy and power densities, it could also increase the net output due to an even larger reduction in the leakage current.<sup>13</sup> One can also decrease the time during which the pyroelectric element is subjected to high temperatures and voltages (process 3–4).<sup>13,30</sup> Material preparation also plays an important role in reducing leakage current by increasing electrical resistivity. For PVDF-TrFE, and polymeric ferroelectric materials in general, one can bake or vacuum heat the pyroelectric material in order to evaporate all solvents within the material as it contributes to reducing the resistance.<sup>33</sup> Pre-poling the material for a certain amount of time can also reduce the leakage current by increasing the film resistance.<sup>34,79</sup> Finally, Maintaining a nonzero electric field can be used to keep the pyroelectric element properly poled during the cooling process 1–2 in the Olsen cycle.<sup>29,30,33,34,83,86</sup>

Sample durability is also a major concern in implementing the Olsen cycle in a device. Indeed, the Olsen cycle performed on a given material requires the cold and hot source temperatures and the electric field span  $E_H - E_L$  to be significant in order to generate energy. However, thermoelectrical cycling over large temperature and electric field ranges may result in excessive thermomechanical stress and premature breakdown of the material. It can be improved by increasing the electrical breakdown strength of the material. For example, samples can be (i) prestressed, such as in thin layer unimorph ferroelectric

driver and sensor actuators to increase sample durability,<sup>163</sup> or (ii) fabricated into single or multilayer thin film capacitors with thickness on the order of nanometers to increase the applied electric field without sample failure.<sup>50</sup>

Moreover, the Sawyer-Tower circuit typically used with the Olsen cycle (Fig. 17) does not harvest the generated energy. This is due to the fact that the power supply used to apply the electric fields  $E_L$  and  $E_H$  required for the cycle is not electrically isolated from the storage capacitor  $C_1$ . Advances in electric circuit are necessary for simultaneously applying the desired bias field and harvesting, i.e., rectifying and storing, the generated power.<sup>88,89,126</sup>

Finally, improvements in the pyroelectric element and electrode geometry discussed in Section 3.1.4 for linear pyroelectric energy conversion could be used in devices implementing pyroelectric energy conversion cycles.<sup>30,113</sup> Recent studies have also focused on improving pyroelectric energy conversion cycles.<sup>119,147,164</sup> First, Zhang et al.<sup>119</sup> conceived a cycle similar to the Olsen cycle by replacing the heating/cooling processes with application of a compressive stress at constant temperature throughout the cycle. They termed this cycle the piezoelectric Ericsson cycle. They demonstrated the cycle on soft PZT samples at 0.1 Hz with electric field  $E_H$  up to 0.3 MV/m and compressive stress up to 50 MPa, presumably at room temperature. Around the same time, McKinley et al.<sup>147</sup> developed and experimentally demonstrated a thermally-biased mechanical energy conversion cycle on PMN-28PT at 1 Hz and at a biased temperature  $T_b \sim 80^\circ\text{C}$  slightly below Curie temperature to take advantage of power generation across the ferroelectric to paraelectric phase transition. Their cycle operated around 1 Hz and featured material efficiency  $\eta_m$  of up to 87%. More recently, Patel et al.<sup>150</sup> estimated the energy density from the same cycle using D-E loops measured under different compressive stresses for PZT<sup>150</sup> and PMN-32PT.<sup>165</sup> In addition, Kim et al.<sup>164</sup> conceived an improvement to the Olsen cycle consisting of adding a process between processes 1–2 and 2–3 during which the pyroelectric material is temporarily electrically isolated prior to and during heating. Ideally, the electric displacement remains constant while the electric field increases during this process. Then, reconnecting the material to the circuit causes the electric displacement and electric field to become the same as they would be at state 3 of the Olsen cycle. This cycle was demonstrated experimentally using PZT ceramics by adding a switch and a diode to a Sawyer-Tower circuit (Fig. 17).<sup>164</sup> Kim et al.<sup>164</sup> were able to generate 160 mW/L corresponding to a 30% increase in the power density generated by the Olsen cycle for identical operating conditions.

## 5. CONCLUSION

Pyroelectric energy conversion has been the subject of intense studies in recent years. Significant progress has been made in a wide range of areas, including: (i) the synthesis, characterization, and identification of promising pyroelectric materials, (ii) improvements in our understanding of the physical phenomena and of different strategies to increase the electrical output and efficiency, and (iii) the design, manufacturing, and assembly of pyroelectric devices. Further interdisciplinary research efforts are needed to make pyroelectric energy conversion a viable technology able to compete with other waste heat energy conversion technologies, such as thermoelectrics and organic Rankine cycles. In particular, material

and device optimizations have yet to be undertaken, and electric circuits specifically designed to condition and store the pyroelectric energy generated are also needed. Finally, it would be useful to assess this technology through the prism of life cycle assessment given the low-grade waste heat it aims to convert and the relatively modest efficiency.

## ACKNOWLEDGMENTS

Parts of this work were funded by (i) the Office of Naval Research under Grant No. N000140710671 (Program manager: Mark Spector), (ii) National Science Foundation IGERT program Clean Energy for Green Industry at UCLA (Grant No. DGE-0903720), and (iii) the NSF-IGERT Materials Training Program (Grant No. DGE-0114443). The authors also thank Randall Olsen for useful discussions and exchange of information early on in their efforts.

## REFERENCES

1. LLNL/DOE, *Lawrence Livermore National Laboratory and Department of Energy*, U.S. Energy Flow Trends—2012, May 2013.
2. Shioji, M., Ishiyama, T., Ikegami, M., Mitani, S., and Shibata, H., Performance and Exhaust Emissions in a Natural-Gas Fueled Dual-Fuel Engine, *JSME Int. J. Series B*, vol. 44, no. 4, pp. 641–648, 2001.
3. Taylor, C. F., *The Internal Combustion Engine in Theory and Practice*, Chapter 8: Heat Losses, MIT Press, Cambridge, MA, 1985.
4. Liu, B. T., Chien, K. H., and Wang, C. C., Effect of Working Fluids on Organic RANkine Cycle for Waste Heat Recovery, *Energy*, vol. 29, no. 8, pp. 1207–1217, 2004.
5. Thombare, D. G. and Verma, S. K., Technological Development in the Stirling Cycle Engines, *Renew. Sustain. Energy Rev.*, vol. 12, pp. 1–38, 2008.
6. Riffat, S. B. and Ma, X., Thermoelectrics: A Review of Present and Potential Applications, *Appl. Thermal Eng.*, vol. 23, pp. 913–935, 2003.
7. Turner, W. C. and Doty, S., *Energy Management Handbook*, 6th ed., Fairmont Press, Lilburn, GA, 2007.
8. Chen, H., Goswami, D. Y., and Stefanakos, E. K., A Review of Thermodynamic Cycles and Working Fluids for the Conversion of Low-Grade Heat, *Renew. Sustain. Energy Rev.*, vol. 14, pp. 3059–3067, 2010.
9. Zebarjadi, M., Esfarjani, K., Dresselhaus, M. S., Ren, Z. F., and Chen, G., Perspectives on Thermoelectrics: From Fundamentals to Device Applications, *Energy Env. Sci.*, vol. 5, pp. 5147–5162, 2012.
10. Lang, S. B., *Sourcebook of Pyroelectricity*, Gordon and Breach, Science Publishers, New York, 1974.
11. Lang, S. B. and Das-Gupta, D. K., *Handbook of Advanced Electronic and Photonic Materials and Devices*, Vol. 4, Academic Press, San Diego, 2001.
12. Lang, S. B., Pyroelectricity: From Ancient Curiosity to Modern Imaging Tool, *Phys. Today*, vol. 58, pp. 31–36, 2005.

13. Ikura, M., Conversion of Low-Grade Heat to Electricity Using Pyroelectric Copolymer, *Ferroelectrics*, vol. 267, pp. 403–408, 2002.
14. Itskovsky, M. A., Pyroelectric Hysteresis Loop at Ferroelectric Phase Transition, *J. Appl. Phys.*, vol. 85, pp. 4256–4258, 1999.
15. Whatmore, R. W., Pyroelectric Devices and Materials, *Rep. Progress Phys.*, vol. 49, pp. 1335–1386, 1986.
16. Brown, C., Kell, R., Taylor, R., and Thomas, L., Piezoelectric Materials, a Review of Progress, *IRE Trans. Compon. Parts*, vol. 9, no. 4, pp. 193–211, 1962.
17. Balta Calleja, F. J., Gonzalez Arche, A., Ezquerro, T. A., Santa Cruz, C., Batallan, F., Frick, B., and Lopez Cabarcos, E., Structure and Properties of Ferroelectric Copolymers of Poly (Vinylidene Fluoride), *Adv. Polym. Sci.*, vol. 108, pp. 1–48, 1993.
18. IEEE Standard on Piezoelectricity, ANSI/IEEE Std. 176-1987, 1988.
19. Lines, M. E. and Glass, A. M., *Principles and Applications of Ferroelectrics and Related Materials*, Clarendon Press, Oxford, UK, 1977.
20. Bao, H. M., Song, J. F., Zhang, J., Shen, Q. D., Vang, C. Z., and Zhang, Q. M., Phase Transitions and Ferroelectric Relaxor Behavior in P(VDF-TrFE-CFE) Terpolymers, *Macromolecules*, vol. 40, pp. 2371–2379, 2007.
21. McLaughlin, E. A., Liu, T., and Lynch, C. S., Relaxor Ferroelectric PMN-32PT Crystals under Stress, Electric Field and Temperature Loading: II-33-Mode Measurements, *Acta Mater.*, vol. 53, no. 14, pp. 4001–4008, 2005.
22. Srivastava, N. and Wang, G. J., A Theory of Double Hysteresis for Ferroelectric Crystals, *J. Appl. Phys.*, vol. 99, p. 054103, 2006.
23. Li, Z., Xi, Z., Xu, Z., and Yao, X., Dielectric/Ferroelectric Response and Phase Transition of PMN-0.32PT Single Crystal, *J. Mater. Sci. Lett.*, vol. 21, pp. 1325–1327, 2002.
24. Bar-Chaim, N., Brunstein, M., Grünberg, J., and Seidman, A., Electric Field Dependence of the Dielectric Constant of PZT Ferroelectric Ceramics, *J. Appl. Phys.*, vol. 45, no. 6, pp. 2398–2405, 1974.
25. Yamada, T., Ueda, T., and Kitayama, T., Ferroelectric-to-Paraelectric Phase Transition of Vinylidene Fluoride-Trifluoroethylene Copolymer, *J. Appl. Phys.*, vol. 52, pp. 948–952, 1981.
26. Hooker, M. W., Properties of PZT-Based Piezoelectric Ceramics between –150 and 250°C, Tech. Rep. NASA contractor report 1998-208708, NASA, Hampton, VA, 1998.
27. Herklotz, A., Plumhof, J. D., Rastelli, A., Schmidt, O. G., Schultz, L., and Dorr, K., Electrical Characterization of PMN-28%PT(001) Crystals Used as Thin-Film Substrates, *J. Appl. Phys.*, vol. 108, p. 094101, 2010.
28. Wan, Q., Chen, C., and Shen, Y. P., Effects of Stress and Electric Field on the Electromechanical Properties of  $\text{Pb}(\text{Mg}_{1/3}\text{Nb}_{2/3})\text{O}_3$ -0.32 $\text{PbTiO}_3$  Single Crystals, *J. Appl. Phys.*, vol. 97, p. 024103, 2005.
29. Navid, A. and Pilon, L., Pyroelectric Energy Harvesting Using Olsen Cycle in Purified and Porous Poly (Vinylidene Fluoride-Trifluoroethylene) [P(VDF-TrFE)] Thin Films, *Smart Mater. Struct.*, vol. 20, p. 025012, 2011.
30. Nguyen, H., Navid, A., and Pilon, L., Pyroelectric Energy Converter Using Co-Polymer P(VDF-TrFE) and Olsen Cycle for Waste Heat Energy Harvesting, *Appl. Thermal Eng.*, vol. 30, no. 14-15, pp. 2127–2137, 2010.

31. Sencadas, V., Lanceros-Mendez, S., and Mano, J. F., Characterization of Poled and Non-Poled  $\beta$ -PVDF Films Using Thermal Analysis Techniques, *Thermocim. Acta*, vol. 424, pp. 201–207, 2004.
32. Kim, K. J. and Kim, G. B., Curie Transition, Ferroelectric Crystal Structure and Ferroelectricity of VDF/TrFE (75/25) Copolymer: 2. The Effect of Poling on Curie Transition and Ferroelectric Crystal Structure, *J. Polym. Sci.*, vol. 38, pp. 4881–4889, 1997.
33. Olsen, R. B., Bruno, D. A., and Briscoe, J. M., Pyroelectric Conversion Cycle of Vinylidene Fluoride-Trifluoroethylene Copolymer, *J. Appl. Phys.*, vol. 57, pp. 5036–5042, 1985.
34. Navid, A., Lynch, C. S., and Pilon, L., Purified and Porous Poly (Vinylidene Fluoride-Trifluoroethylene) Thin Films for Pyroelectric Infrared Sensing and Energy Harvesting, *Smart Mater. Struct.*, vol. 19, p. 055006, 2010.
35. Cuadras, A., Gasulla, M., and Ferrari, V., Thermal Energy Harvesting through Pyroelectricity, *Sen. Actuators A*, vol. 158, no. 1, pp. 132–139, 2010.
36. Zhang, R., Jiang, B., and Cao, W., Orientation Dependence of Piezoelectric Properties of Single Domain  $0.67\text{PbMg}_{1/3}\text{Nb}_{2/3}\text{O}_3$ - $0.33\text{PbTiO}_3$  Single Crystals, *Appl. Phys. Lett.*, vol. 82, no. 21, pp. 3737–3739, 2003.
37. Li, Z., Xu, Z., Xi, Z., Xiang, F., and Yao, X., Thermal Expansion Characteristics in [001]-Oriented PMN-0.32PT Single Crystals, *Ferroelectrics*, vol. 355, no. 1, pp. 245–251, 2007.
38. Kumar, R., Molin, D., Young, L., and Ke, F., New High Temperature Polymer Thin Coating for Power Electronics, in *Proceedings of 19th Applied Power Electronics Conference and Exposition*, Vol. 2, Annual IEEE, pp. 1247–1249, 2004.
39. Yasuda, N., Banno, T., Fujita, K., Ohwa, H., Matushita, M., Yamashita, Y., Iwata, M., and Ishibashi, Y., Piezoelectric Properties of Relaxor Ferroelectric Solid Solution Single Crystals PMN-PT and PZN-PT near MPB under Pressures, *Ferroelectrics*, vol. 347, no. 1, pp. 44–49, 2007.
40. Varma, K. B. R., Morphology and Dielectric Properties of Fish Scales, *Curr. Sci.*, vol. 59, no. 8, pp. 420–423, 1990.
41. Shindo, Y. and Narita, F., Piezomechanics in PZT Stack Actuators for Cryogenic Fuel Injectors, in *Smart Actuation and Sensing Systems*, Berselli, G., Vertechy, R., and Vassura, G., (eds.), Chap. 24, InTech, Rijeka, Croatia, 2012.
42. Park, S. E. and Shrout, T. R., Ultrahigh Strain and Piezoelectric behavior in Relaxor Based Ferroelectric Single Crystals, *J. Appl. Phys.*, vol. 82, no. 4, pp. 1804–1811, 1997.
43. Samara, G. A., Ferroelectricity Revisited—Advances in Materials and Physics, *Solid State Physics*, vol. 56, pp. 239–458, 2001.
44. Haertling, G. H. and Buchanan, R. C. (eds.), *Ceramic Materials for Electronics: Processing, Properties, and Applications*, Marcel Dekker, New York, 1991.
45. Akbas, M., Reaney, I., and Lee, W., Domain Structure-Property Relations in Lead Lanthanum Zirconate Titanate Ceramics, *J. Mater. Res.*, vol. 11, no. 9, pp. 2293–2301, 1996.
46. Lynch, C. S., The Effect of Uniaxial Stress on the Electro-Mechanical Response of 8/65/35 PLZT, *Acta Materialia*, vol. 44, pp. 4137–4139, 1996.
47. Liu, T. and Lynch, C. S., Domain Engineered Relaxor Ferroelectric Single Crystals, *Continuum Mech. Thermodyn.*, vol. 18, pp. 119–135, 2006.
48. Lynch, C. S., Large Field Electromechanical Measurement Techniques for Ferroelectric Ma-

- terials, *Integr. Ferroelect.*, vol. 111, pp. 59–67, 2011.
49. Haertling, G. H., Ferroelectric Ceramics: History and Technology, *J. Am. Ceram. Soc.*, vol. 82, no. 4, pp. 797–818, 1999.
  50. Dausch, D. E. and Haertling, G. H., The Domain Switching and Structural Characteristics of PLZT Bulk Ceramics and Thin Films Chemically Prepared from the Same Acetate Precursor Solutions, *J. Mater. Sci.*, vol. 31, pp. 3409–3417, 1996.
  51. Haertling, G. H. and Land, C. E., Hot-Pressed (Pb,La)(Zr,Ti)O<sub>3</sub> Ferroelectric Ceramics for Electro-Optic Applications, *J. Am. Ceram. Soc.*, vol. 54, no. 1, pp. 1–11, 1971.
  52. Bobnar, V., Kutnjak, Z., Pirc, R., and Levstik, A., Electric-Field-Temperature Phase Diagram of the Relaxor Ferroelectric Lanthanum-Modified Lead Zirconate Titanate, *Phys. Rev. B*, vol. 60, pp. 6420–6427, 1999.
  53. Vodopivec, B., Filipic, C., Levstik, A., Holc, J., and Kutnjak, Z., E-T Phase Diagram of the 6.5/65/35 PLZT Incipient Ferroelectric, *J. Eur. Ceram. Soc.*, vol. 24, pp. 1561–1564, 2004.
  54. Viehland, D., Dai, X. H., Li, J. F., and Xu, Z., Effects of Quenched Disorder on La-Modified Lead Zirconate Titanate: Long and short-Range Ordered Structurally Incommensurate Phases, and Glassy Polar Clusters, *J. Appl. Phys.*, vol. 84, no. 1, pp. 458–471, 1998.
  55. Kamba, S., Bovton, V., Petzelt, J., Rychetsky, I., Mizaras, R., Brilingas, A., Banys, J., Gringas, J., and Kosec, M., Dielectric Dispersion of the Relaxor PLZT Ceramics in the Frequency Range 20 Hz–100 THz, *J. Phys.: Condens. Matter*, vol. 12, pp. 497–519, 2000.
  56. Dellis, J. L., El Marssi, M., Tilloloy, P., Farhi, R., and Viehland, D., A Dielectric Study of the x/65/35 Lanthanum-Modified Lead Zirconate Titanate Series, *Ferroelectrics*, vol. 201, pp. 167–174, 1997.
  57. Xi, Y., Zhili, C., and Cross, L. E., Polarization and Depolarization behavior of Hot Pressed Lead Lanthanum Zirconate Titanate Ceramics, *J. Appl. Phys.*, vol. 54, no. 6, pp. 3399–3403, 1983.
  58. Divya, A. S. and Kumar, V., A Novel Mechanism for Relaxor-Ferroelectric Transition in PLZT (8/65/35), *J. Am. Ceram. Soc.*, vol. 92, no. 9, pp. 2029–2032, 2009.
  59. Kutnjak, Z., Filipic, C., Pirc, R., and Levstik, A., Slow Dynamics and Ergodicity Breaking in a Lanthanum-Modified Lead Zirconate Titanate Relaxor System, *Phys. Rev. B*, vol. 59, no. 1, pp. 294–301, 1999.
  60. Lee, F. Y., Jo, H. R., Lynch, C. S., and Pilon, L., Pyroelectric Energy Conversion Using PLZT Ceramics and Ferroelectric-Ergodic Relaxor Phase Transition, *Smart Mater. Struct.*, vol. 22, no. 2, p. 025038, 2013.
  61. Colla, E. V., Yushin, N. K., and Viehland, D., Dielectric Properties of (PMN)<sub>1-x</sub>(PT)<sub>x</sub>, *J. Appl. Phys.*, vol. 83, no. 6, pp. 3298–3304, 1998.
  62. Ye, Z.-G. and Dong, M., Morphotropic Domain Structures and Phase Transitions in Relaxor-Based Piezo-Ferroelectric (1-x)PbMg<sub>1/3</sub>Nb<sub>2/3</sub>O<sub>3</sub>-xPbTiO<sub>3</sub> Single Crystals, *J. Appl. Phys.*, vol. 87, no. 5, pp. 2312–2319, 2000.
  63. Viehland, D. and Powers, J., Electromechanical Coupling Coefficient of <001>-Oriented of Pb(Mg<sub>1/3</sub>Nb<sub>2/3</sub>)O<sub>3</sub>-PbTiO<sub>3</sub> Crystals: Stress and Temperature Independence, *Appl. Phys. Lett.*, vol. 78, pp. 3112–3114, 2001.
  64. McLaughlin, E. A., Liu, T., and Lynch, C. S., Relaxor Ferroelectric PMN-32PT Crystals under Stress And Electric Field Loading: I-32 Mode Measurements, *Acta Mater.*, vol. 52, pp.

- 3849–3857, 2004.
65. Viehland, D., Li, J., McLaughlin, E. A., Powers, J., Janus, R., and Robinson, H., Effect of Uniaxial Stress on the Large-Signal Electromechanical Properties of Electrostrictive and Piezoelectric Lead Magnesium Niobate Lead Titanate Ceramics, *Appl. Phys. Lett.*, vol. 95, pp. 1969–1972, 2004.
  66. Feng, Z., Lin, D., Luo, H., Li, S., and Fang, D., Effect of Uniaxial Stress on the Electromechanical Response of  $\langle 001 \rangle$ -Oriented  $\text{Pb}(\text{Mg}_{1/3}\text{Nb}_{2/3})\text{O}_3$ - $\text{PbTiO}_3$  Crystals, *J. Appl. Phys.*, vol. 97, p. 024103, 2005.
  67. Zhou, D., Wang, F., Luo, L., Chen, J., Ge, W., Zhao, X., and Luo, H., Characterization of Complete Electromechanical Constants of Rhombohedral  $0.72\text{Pb}(\text{Mg}_{1/3}\text{Nb}_{2/3})$ - $0.28\text{PbTiO}_3$  Single Crystals, *J. Phys. D*, vol. 41, p. 185402, 2008.
  68. Tang, Y. and Luo, H., Investigation of the electrical properties of  $(1-x)\text{Pb}(\text{Mg}_{1/2}\text{Nb}_{2/3})\text{O}_3$ - $x\text{PbTiO}_3$  single crystals with special reference to pyroelectric detection, *J. Phys. D*, vol. 42, p. 075406, 2009.
  69. Kamzina, L. S. and Luo, H., Influence of the Electric Field on Structural Transformations and Phase Boundary for  $\text{PMg}_{1/3}\text{Nb}_{2/3}\text{O}_3$ - $x\text{PbTiO}_3$  Single Crystals, *Phys. Solid State*, vol. 51, no. 11, pp. 2316–2323, 2009.
  70. Li, Z., Xi, Z., Xu, Z., and Yao, X., Dielectric/Ferroelectric Response and Phase Transition of  $\text{PMN}0.32\text{PT}$  Single Crystal, *J. Mater. Sci. Lett.*, vol. 21, no. 17, pp. 1325–1327, 2002.
  71. Tu, C.-S., Tsai, C.-L., Schmidt, V. H., Luo, H., and Yin, Z., Dielectric, Hypersonic, and Domain Anomalies of  $(\text{PbMg}_{1/3}\text{Nb}_{2/3}\text{O}_3)_{1-x}(\text{PbTiO}_3)_x$  Single Crystals, *J. Appl. Phys.*, vol. 89, no. 12, pp. 7908–7916, 2001.
  72. Guo, Y., Luo, H., Ling, D., Xu, H., He, T., and Yin, Z., The Phase Transition Sequence and the Location of the Morphotropic Phase Boundary Region in  $(1-x)\text{Pb}(\text{Mg}_{1/3}\text{Nb}_{2/3})\text{O}_3$ - $x\text{PbTiO}_3$  Single Crystal, *J. Phys.: Condens. Matter*, vol. 15, pp. L77–L82, 2003.
  73. Han, J. and Cao, W., Electric field effects on the Phase Transitions in  $[001]$ -Oriented  $(1-x)\text{Pb}(\text{Mg}_{1/3}\text{Nb}_{2/3})\text{O}_3$ - $x\text{PbTiO}_3$  Single Crystals with Compositions near the Morphotropic Phase Boundary, *Phys. Rev. B*, vol. 68, p. 134102, 2003.
  74. McKinley, I., *Thermomechanical Energy Conversion Using Ferroelectric Materials*, PhD thesis, UCLA, 2013.
  75. Merz, W. J., Double Hysteresis Loop of  $\text{BaTiO}_3$  at the Curie Point, *Phys. Rev.*, vol. 91, pp. 513–517, 1953.
  76. Chu, B., Zhou, X., Ren, K., Neese, B., Lin, M., Wang, Q., Bauer, F., and Zhang, Q. M., A Dielectric Polymer with High Electric Energy Density and Fast Discharge Speed, *Science*, vol. 313, pp. 334–336, 2006.
  77. Yang, D., Tornga, S., Orler, B., and Welch, C., Aging of Poly (Vinylidene Fluoride) Hollow Fibers in Light Hydrocarbon Environments, *J. Membr. Sci.*, vol. 409–410, pp. 302–317, 2012.
  78. Kim, K. J. and Hsu, S. L., An Infra-Red Spectroscopic Study of Structural Reorganization of a Uniaxially Draw VDF/TrFE Copolymer in an Electric Field, *J. Polym. Sci.*, vol. 35, pp. 3612–3618, 1993.
  79. Kouchachvili, L. and Ikura, M., Pyroelectric Conversion-Effects of P(VDF-TrFE) Preconditioning on Power Conversion, *J. Electrostat.*, vol. 65, pp. 182–188, 2007.
  80. Bauer, S. and Lang, S. B., Pyroelectric Polymer Electrets, *IEEE Trans. Dielec. Elect. Insulat.*,

- vol. 56, pp. 57–62, 1996.
81. Olsen, R. B., Bruno, D. A., and Briscoe, J. M., Pyroelectric Conversion Cycles, *J. Appl. Phys.*, vol. 58, pp. 4709–4716, 1985.
  82. Teyssedre, G., Bernes, A., and Lacabanne, C., Cooperative Movements Associated with the Curie Transition in P(VDF-TrFE) Copolymers, *J. Polym. Sci. Part B: Polymer Physics*, vol. 33, no. 6, pp. 879–890, 1995.
  83. Olsen, R. B. and Bruno, D. A., Pyroelectric Conversion Materials, in *Proceedings of 21st Intersociety Energy Conversion Engineering Conference*, American Chemical Society, San Diego, pp. 89–93, Aug. 25–29, 1986.
  84. Yamazaki, H., Ohwaki, J., Yamada, T., and Kitayama, T., Temperature Dependence of the Pyroelectric Response of Vinylidene Fluoride Trifluoroethylene Copolymer and the Effect of Its Poling Conditions, *Appl. Phys. Lett.*, vol. 39, pp. 772–773, 1981.
  85. Yu, J. and Ikura, M., Direct Conversion of Low-Grade Heat to Electricity Using Pyroelectric Conversion, in *Proceedings of 4th IASTED International Conference European Power and Energy Systems*, Rhodes, Greece, pp. 442–446, 2004.
  86. Kouchachvili, L. and Ikura, M., Improving the Efficiency of Pyroelectric Conversion, *Int. J. Energy Res.*, vol. 32, pp. 328–335, 2008.
  87. Kouchachvili, L. and Ikura, M., High Performance P(VDF-TrFE) Copolymer for Pyroelectric Conversion, U. S. Patent No. 7,323,506, 2006.
  88. Sebald, G., Guyomar, D., and Agbossou, A., On Thermoelectric and Pyroelectric Energy Harvesting, *Smart Mater. Struct.*, vol. 18, p. 125006, 2009.
  89. Guyomar, D., Sebald, G., Lefeuvre, E., and Khodayari, A., Toward heat Energy Harvesting Using Pyroelectric Materials, *J. Intell. Mater. Syst. Struct.*, vol. 20, no. 3, pp. 265–271, 2009.
  90. Hsiao, C.-C. and Jhang, J.-W., Pyroelectric Harvesters for Generating Cyclic Energy, *Energies*, vol. 8, no. 5, pp. 3489–3502, 2015.
  91. Hsiao, C.-C., Jhang, J.-W., and Siao, A.-S., Study on Pyroelectric Harvesters Integrating Solar Radiation with Wind Power, *Energies*, vol. 8, no. 7, pp. 7465–7477, 2015.
  92. Sebald, G., Seveyrat, L., Guyomar, D., Lebrun, L., Guiffard, B., and Pruvost, S., Electrocaloric and Pyroelectric Properties of  $0.75\text{Pb}(\text{Mg}_{1/3}\text{Nb}_{2/3})\text{O}_3\text{-}0.25\text{PbTiO}_3$  Single Crystals, *J. Appl. Phys.*, vol. 100, p. 124112, 2006.
  93. Sebald, G., Lefeuvre, E., and Guyomar, D., Pyroelectric Energy Conversion: Optimization Principles, *IEEE Trans. Ultrason. Ferroelec. Freq. Control*, vol. 55, pp. 538–551, 2008.
  94. Bowen, C. R., Taylor, J., Le, E., Boulbar, Zabek, D., and Topolov, V. Yu., A Modified Figure of Merit for Pyroelectric Energy Harvesting, *Mater. Lett.*, vol. 138, pp. 243–246, 2015.
  95. Mane, P., Xie, J., Leang, K., and Mossi, K., Cyclic Energy Harvesting from Pyroelectric Materials, *IEEE Trans. Ultrason. Ferroelec. Freq. Control*, vol. 58, no. 1, pp. 10–17, 2011.
  96. Hsiao, C.-C., Siao, A.-S., and Ciou, J.-C., Improvement of Pyroelectric Cells for Thermal Energy Harvesting, *Sensors*, vol. 12, no. 1, pp. 534–548, 2012.
  97. Xie, J., Mane, X. P., Green, C. W., Mossi, K. M., and Kam Leang, K., Performance of Thin Piezoelectric Materials for Pyroelectric Energy Harvesting, *J. Intell. Mater. Syst. Struct.*, vol. 21, no. 3, pp. 243–249, 2010.
  98. Ravindran, S. K. T., Kroener, M., and Woias, P., A Bimetallic Micro Heat Engine for Pyroelectric Energy Conversion, *Procedia Eng.*, vol. 47, pp. 33–36, 2012.

99. Zhang, Q., Agbossou, A., Feng, Z., and Cosnier, M., Solar Micro-Energy Harvesting with Pyroelectric Effect and Wind Flow, *Sens. Actuators A*, vol. 168, no. 2, pp. 335–342, 2011.
100. Krishnan, S. H., Ezhilarasi, D., Uma, G., and Umopathy, M., Pyroelectric-Based Solar and Wind Energy Harvesting System, *IEEE Trans. Sustainable Energy*, vol. 5, no. 1, pp. 73–81, 2014.
101. Leng, Q., Chen, L., Guo, H., Liu, J., Liu, G., Hu, C., and Xi, Y., Harvesting Heat Energy from Hot/Cold Water with a Pyroelectric Generator, *J. Mater. Chem. A*, vol. 2, pp. 11940–11947, 2014.
102. Erturun, U., Green, C., Richeson, M. L., and Mossi, K., Experimental Analysis of Radiation Heat Based Energy Harvesting through Pyroelectricity, *J. Intell. Mater. Syst. Struct.*, vol. 25, no. 14, pp. 1838–1849, 2014.
103. Hsiao, C.-C. and Siao, A.-S., Improving Pyroelectric Energy Harvesting Using a Sandblast Etching Technique, *Sensors*, vol. 13, no. 9, pp. 12113–12131, 2013.
104. Leng, Q. and Hu, C., Question Regarding Paper Published, *Mat. J. Chem. A*, vol. 2, no. 30, pp. 11940–11947, 2014.
105. Hsiao, C.-C., Ciou, J.-C., Siao, A.-S., and Lee, C.-Y., Temperature Field Analysis for PZT Pyroelectric Cells for Thermal Energy Harvesting, *Sensors*, vol. 11, no. 11, pp. 10458–10473, 2011.
106. Ravindran, S. K. T., Huesgen, T., Kroener, M., and Woias, P., A Self-Sustaining Micro Thermomechanic-Pyroelectric Generator, *Appl. Phys. Lett.*, vol. 99, no. 10, p. 104102, 2011.
107. Batra, A. K., Bandyopadhyay, A., Chilvery, A. K., and Thomas, M., Modeling and Simulation for PVDF-Based Pyroelectric Energy Harvester, *Energy Sc. Technol.*, vol. 5, no. 2, pp. 1–7, 2013.
108. Clingman, W. H. and Moore, R. G., Application of Ferroelectricity to Energy Conversion Processes, *J. Appl. Phys.*, vol. 32, pp. 675–681, 1961.
109. Fatuzzo, E., Kiess, H., and Nitsche, R., Theoretical Efficiency of Pyroelectric Power Converters, *J. Appl. Phys.*, vol. 37, pp. 510–516, 1966.
110. van der Ziel, A., Solar Power Generation with the Pyroelectric Effect, *J. Appl. Phys.*, vol. 45, p. 4128, 1974.
111. Hoh, S. R., Conversion of Thermal to Electrical Energy with Ferroelectric Materials, *Proc. IEEE*, vol. 51, pp. 838–845, 1963.
112. Childress, J. D., Application of a Ferroelectric Material in an Energy Conversion Device, *J. Appl. Phys.*, vol. 33, pp. 1793–1798, 1962.
113. Olsen, R. B., Bruno, D. A., Briscoe, J. M., and Butler, W. F., A Pyroelectric Energy Converter which Employs Regeneration, *Ferroelectrics*, vol. 38, pp. 975–978, 1981.
114. Olsen, R. B., Ferroelectric Conversion of Heat to Electrical Energy—A Demonstration, *J. Energy*, vol. 6, pp. 91–95, 1982.
115. Olsen, R. B. and Brown, D. D., High-Efficiency Direct Conversion of Heat to Electrical Energy—Related Pyroelectric Measurements, *Ferroelectrics*, vol. 40, pp. 17–27, 1982.
116. Olsen, R. B. and Evans, D., Pyroelectric Energy Conversion: Hysteresis Loss and Temperature Sensitivity of a Ferroelectric Material, *J. Appl. Phys.*, vol. 54, pp. 5941–5944, 1983.
117. Olsen, R. B., Bruno, D. A., and Briscoe, J. M., Cascaded Pyroelectric Energy Converter, *Ferroelectrics*, vol. 59, pp. 205–219, 1984.

118. Sebald, G., Pruvost, S., and Guyomar, D., Energy Harvesting Based on Ericsson Pyroelectric Cycles in a Relaxor Ferroelectric Ceramic, *Smart Mater. Struct.*, vol. 17, pp. 1–6, 2008.
119. Zhang, B., Ducharme, B., Guyomar, D., and Sebald, G., Energy Harvesting Based on Piezoelectric Ericsson Cycles in a Piezoceramic Material, *Eur. Phys. J. Special Top.*, vol. 222, no. 7, pp. 1733–1743, 2013.
120. Bhatia, B., Damodaran, A. R., Cho, H., Martin, L. W., and King, W. P., High-Frequency Thermal-Electrical Cycles for Pyroelectric Energy Conversion, *J. Appl. Phys.*, vol. 116, p. 194509, 2014.
121. Olsen, R. B., Apparatus and Method for Pyroelectric Power Conversion, U.S. Patent No. 4,425,540, Jan. 10, 1984.
122. Olsen, R. B., Pyroelectric Energy Converter Element Comprising Vinylidene Fluoride-Trifluoroethylene Copolymer, U.S. Patent No. 4,620,262, Oct. 28, 1986.
123. Olsen, R. B., Pyroelectric Energy Converter and Method, U.S. Patent No. 4,647,836, Mar. 3, 1987.
124. Vats, G., Vaish, R., and Bowen, C. R., An Analysis of Lead-Free  $(\text{Bi}_{0.5}\text{Na}_{0.5})_{0.915}(\text{Bi}_{0.5}\text{K}_{0.5})_{0.05}\text{Ba}_{0.02}\text{Sr}_{0.015}\text{TiO}_3$  Ceramic for Efficient Refrigeration and Thermal Energy Harvesting, *Mater. Res. Express*, vol. 1, p. 025504, 2014.
125. Lee, F. Y., Goljahi, S., McKinley, I. M., Lynch, C. S., and Pilon, L., Pyroelectric Waste Heat Energy Harvesting Using Relaxor Ferroelectric 8/65/35 PLZT and the Olsen Cycle, *Smart Mater. Struct.*, vol. 21, p. 025021, 2012.
126. Cha, G. and Ju, Y. S., Pyroelectric Energy Harvesting Using Liquid-Based Switchable Thermal Interfaces, *Sens. Actuators A*, vol. 189, pp. 100–107, 2013.
127. Kandilian, R., Navid, A., and Pilon, L., Pyroelectric Energy Harvesting Capabilities of PMN-PT near the Morphotropic Phase Boundary, *Smart Mater. Struct.*, vol. 20, no. 5, p. 055020, 2011.
128. McKinley, I. M. and Pilon, L., Phase Transitions and Thermal Expansion in Pyroelectric Energy Conversion, *Appl. Phys. Lett.*, vol. 102, p. 023906, 2013.
129. McKinley, I. M., Kandilian, R., and Pilon, L., Waste Heat Energy Harvesting Using the Olsen Cycle on  $0.945\text{Pb}(\text{Zn}_{1/3}\text{Nb}_{2/3})\text{O}_3$ - $0.055\text{PbTiO}_3$  Single Crystals, *Smart Mater. Struct.*, vol. 21, no. 3, p. 035015, 2012.
130. McKinley, I. M., Lee, F. Y., and Pilon, L., Novel Cycle for Direct Thermomechanical Energy Conversion, *Appl. Energy*, vol. 126, pp. 78–89, 2014.
131. Zhu, H., Pruvost, S., Guyomar, D., and Khodayari, A., Thermal Energy Harvesting From  $\text{Pb}(\text{Zn}_{1/3}\text{Nb}_{2/3})_{0.955}\text{Ti}_{0.045}\text{O}_3$  Single Crystals Phase Transitions, *J. Appl. Phys.*, vol. 106, no. 12, p. 124102, 2009.
132. Chang, C., Tran, V. H., Wang, J., Fuh, Y.-K., and Lin, L., Direct-Write Piezoelectric Polymeric Nanogenerator with High Energy Conversion Efficiency, *Nano Lett.*, vol. 10, pp. 726–731, 2010.
133. Beer, Jr., F. P., Johnston, E. R., and DeWolf, J. T., *Mechanics of Materials*, 4th ed., McGraw-Hill, New York, NY, 2006.
134. Sawyer, C. B. and Tower, C. H., Rochelle Salt as a Dielectric, *Phys. Rev.*, vol. 35, pp. 269–275, 1930.
135. Chin, T., Lee, F. Y., McKinley, I. M., Goljahi, S., Lynch, C. S., and Pilon, L., Pyroelectric

- Waste Heat Energy Harvesting Using 9.5/65/35 PLZT Ceramics, *IEEE Trans. Ultrason. Ferroelect. Freq. Control*, vol. 59, pp. 2373–2385, 2012.
136. Lee, F. Y., Navid, A., and Pilon, L., Pyroelectric Waste Heat Energy Harvesting Using Heat Conduction, *Appl. Thermal Eng.*, vol. 37, pp. 30–37, 2012.
  137. Narayanaswamy, A., Shen, S., and Chen, G., Near-Field Radiative Heat Transfer between a Sphere and a Substrate, *Appl. Phys. B*, vol. 78, p. 115303, 2000.
  138. Shen, S., Narayanaswamy, A., and Chen, G., Surface Phonon Polaritons Mediated Energy Transfer Between Nanoscale Gaps, *Nano Letters*, vol. 9, no. 8, pp. 2909–2913, 2009.
  139. Narayanaswamy, A., Shen, S., Hu, L., Chen, X., and Chen, G., Breakdown of the Planck Blackbody Radiation Law at Nanoscale Gaps, *Appl. Phys. A*, vol. 96, no. 2, pp. 357–362, 2009.
  140. Fang, J., Frederich, H., and Pilon, L., Harvesting Nanoscale Thermal Radiation Using Pyroelectric Materials, *ASME J. Heat Tran.*, vol. 132, no. 9, p. 092701, 2010.
  141. Pilon, L., Direct Conversion of Nanoscale Thermal Radiation to Electrical Energy Using Pyroelectric Materials, U.S. Patent App. No. 13/155,288, Dec. 8, 2011.
  142. Carrillo, L. Y. and Bayazitoglu, Y., Near-Field Radiative Heat Exchange Analysis of a Spacecraft Waste Heat Converter Design, *ASME J. Thermal Sci. Eng. Appl.*, vol. 4, no. 2, p. 021001, 2012.
  143. Hunter, S. R., Lavrik, N. V., Bannuru, T., Mostafa, S., Rajic, S., and Datskos, P. G., Development of MEMS Based Pyroelectric Thermal Energy Harvesters, *Proc. SPIE*, vol. 8035, p. 80350V, 2011.
  144. Khodayari, A., Pruvost, S., Sebald, G., Guyomar, D., and Mohammadi, S., Nonlinear Pyroelectric Energy Harvesting from Relaxor Single Crystals, *IEEE Trans. Ultrason. Ferroelec. Freq. Control*, vol. 56, pp. 693–699, 2009.
  145. Lynch, C. S., Fracture of Ferroelectric and Relaxor Electro-Ceramics: Influence of Electric Field, *Acta Mater.*, vol. 46, no. 2, pp. 599–608, 1997.
  146. Cao, H. and Evans, A. G., Electric-Field-Induced Fatigue Crack Growth in Piezoelectrics, *J. Am. Ceram. Soc.*, vol. 77, no. 7, pp. 1783–1786, 1994.
  147. McKinley, I. M., Goljahi, S., Lynch, C. S., and Pilon, L., A Novel Thermally Biased Mechanical Energy Conversion Cycle, *J. Appl. Phys.*, vol. 114, p. 224111, 2013.
  148. Zheng, L., Lu, X., Shang, H., Xi, Z., Wang, R., Wang, J., Zheng, P., and Cao, W., Hysteretic Phase Transition Sequence in  $0.67\text{PbMg}_{1/3}\text{Nb}_{2/3}\text{O}_3$ - $0.33\text{PbTiO}_3$  Single Crystal Driven by Electric Field and Temperature, *Phys. Rev. B*, vol. 91, p. 184105, 2015.
  149. Zheng, X.-C., Zheng, G.-P., Lin, Z., and Jiang, Z.-Y., Thermo-Electrical Energy Conversions in  $\text{Bi}_{0.5}\text{Na}_{0.5}\text{TiO}_3$ - $\text{BaTiO}_3$  Thin Films Prepared by Solgel Method, *Thin Solid Films*, vol. 522, pp. 125–128, 2012.
  150. Patel, S., Chauhan, A., and Vaish, R., Enhanced Energy Harvesting in Commercial Ferroelectric Materials, *Mater. Res. Express*, vol. 1, no. 2, p. 025504, 2014.
  151. Hao, X., Zhao, Y., and An, S., Giant Thermal-Electrical Energy Harvesting Effect of  $\text{Pb}_{0.97}\text{La}_{0.02}(\text{Zr}_{0.75}\text{Sn}_{0.18}\text{Ti}_{0.07})\text{O}_3$  Antiferroelectric Thick Films, *J. Am. Ceram. Soc.*, vol. 98, pp. 361–365, 2015.
  152. Vats, G., Kushwaha, H. S., Vaish, R., Madhar, N. A., Shahabuddin, M., Parakkandy, J. M., and Batoo, K. M., Giant Energy Harvesting Potential in (100)-Oriented  $0.68\text{PbMg}_{1/3}\text{Nb}_{2/3}\text{O}_3$ -

- 0.32PbTiO<sub>3</sub> with Pb(Zr<sub>0.3</sub>Ti<sub>0.7</sub>)O<sub>3</sub>/PbO<sub>x</sub> Buffer Layer and (001)-Oriented 0.67PbMg<sub>1/3</sub>Nb<sub>2/3</sub>O<sub>3</sub>-0.33PbTiO<sub>3</sub> Thin Films, *J. Adv. Dielec.*, vol. 4, p. 1450029, 2014.
153. Vats, G., Kushwaha, H. S., and Vaish, R., Enormous Energy Harvesting and Storage Potential in Multiferroic Epitaxial Thin Film Heterostructures: An Unforeseen Era, *Mat. Res. Express*, vol. 1, no. 1, p. 015503, 2014.
  154. Sao, R., Vats, G., and Vaish, R., A Prime Lead-Free Ferroelectric Ceramic for Thermal Energy Harvesting: 0.88Bi<sub>0.5</sub>Na<sub>0.5</sub>TiO<sub>3</sub>-0.2SrTiO<sub>3</sub>-0.1Bi<sub>0.5</sub>Li<sub>0.5</sub>TiO<sub>3</sub>, *Ferroelectrics*, vol. 474, pp. 1–7, 2015.
  155. Maiwa, H., Jia, T., and Kimura, H., Energy Harvesting Using PLZT and Lead-Free Ceramics and Their Piezoelectric Properties on the Nano-Scale, *Ferroelectrics*, vol. 475, no. 1, pp. 71–81, 2015.
  156. Park, M. H., Kim, H. J., Kim, Y. J., Moon, T., Kim, K. D., and Hwang, C. S., Toward a Multifunctional Monolithic Device Based on Pyroelectricity and the Electrocaloric Effect of Thin Antiferroelectric Hf<sub>x</sub>Zr<sub>1-x</sub>O<sub>2</sub> Films, *Nano Energy*, vol. 12, pp. 131–140, 2015.
  157. Hu, W. J., Juo, D.-M., Wang, J., Chen, Y.-C., Chu, Y.-H., and Wu, T., Universal Ferroelectric Switching Dynamics of Vinylidene Fluoride-Trifluoroethylene Copolymer Films, *Sci. Rep.*, vol. 4, p. 4772, 2014.
  158. Moran, M. J. and Shapiro, H. N., *Fundamentals of Engineering Thermodynamics*, 5th ed., John Wiley and Sons, New York, NY, 2004.
  159. Vanderpool, D., Yoon, J. H., and Pilon, L., Simulations of a Prototypical Device Using Pyroelectric Materials for Harvesting Waste Heat, *Int. J. Heat Mass Transfer*, vol. 51, pp. 5052–5062, 2008.
  160. Navid, A., Vanderpool, D., Bah, A., and Pilon, L., Towards Optimization of a Pyroelectric Energy Converter for Harvesting Waste Heat, *Int. J. Heat Mass Transfer*, vol. 53, no. 19-20, pp. 4060–4070, 2010.
  161. Olsen, R. B., Butler, W. F., Drummond, J. E., Bruno, D. A., and Briscoe, J. M., Heat Flow in a Pyroelectric Converter, in *Proc. of 20th Intersociety Energy Conservation Engineering Conference*, Vol. 3, Miami Beach, pp. 595–602, Nov. 17–22, 1985.
  162. Moreno, R. C., James, B. A., Navid, A., and Pilon, L., Pyroelectric Energy Converter for Harvesting Waste Heat: Simulations Versus Experiments, *Int. J. Heat Mass Transfer*, vol. 55, pp. 4301–4311, 2012.
  163. Webber, K., Hopkinson, D., and Lynch, C., Application of a Classical Lamination Theory Model to the Design of Piezoelectric Composite Unimorph Actuators, *J. Intell. Mater. Syst. Struct.*, vol. 17, pp. 29–34, 2006.
  164. Kim, Y., Kim, J., Yamanaka, S., Nakajima, A., Ogawa, T., Serizawa, T., Tanaka, H., Baba, M., Fukuda, T., Yoshii, K., Takeda, M., Yamada, N., Nakayama, T., and Nihara, K., Novel Electrothermodynamic Power Generation, *Adv. Energy Mater.*, vol. 5, p. 1401942, 2015.
  165. Patel, S., Moghal, A. A. B., Ahamad, N. M., Chauhan, A., and Vaish, R., Cyclic Piezoelectric Energy Harvesting in PMN-PT Single Crystals, *Ferroelectrics*, vol. 481, no. 1, pp. 138–145, 2015.
  166. Zhu, H., Pruvost, S., Cottinet, P. J., and Guyomar, D., Energy Harvesting by Nonlinear Capacitance Variation for a Relaxor Ferroelectric Poly (Vinylidene Fluoride-Trifluoroethylene-Chlorofluoroethylene) Terpolymer, *Appl. Phys. Lett.*, vol. 98, no. 22, p. 222901, 2011.